People's Democratic Republic of Algeria
Ministry of Higher Education and Scientific Research

University M'Hamed BOUGARA – Boumerdes

Institute of Electrical and Electronic Engineering

Department of Electronics

Final Year Project Report Presented in Partial Fulfilment of
the Requirements for the Degree of

MASTER

In **Electronics**

Option: **Computer Engineering**

Title:

Fiber Tracking Post-processing for Abnormal Brain Tissues Analysis using DW-MRI

Presented by:

- **BOUDJEMA Boussaad**
- **HOUFAF Abdessalem**

Supervisor:

Dr. CHERIFI Dalila

Registration Number:……../2020

Dedications

I would like to thank my parents **Ikhlef** and **Nacira** for what they have done for me, my family and all of my friends.

BOUDJEMA Boussaad

I would like to thank my parents **Azzdine** and **Zahia** for what they have done for me, my family and all of my friends.

HOUFAF Abdessalem

Acknowledgements

First and foremost, we would like to express our thanks and deep gratitude to our supervisor Dr. CHERIFI Dalila for her constant support, orientation, advice and encouragement during the accomplishment of this project.

We are very thankful for all our teachers for their efforts that helped us to accumulate our modest knowledge and improve our skill set while studying at IGEE.

Abstract

Tractography represents fiber tracts of the cerebral white matter and their connections in the brain based on Diffusion Weighted Magnetic Resonance Imaging (DW-MRI), which can reveal abnormalities in the white matter especially in fibers' structure.

While this technique is very useful in getting a 3d model of the brain's neural circuits, it still has some important limitations as it produces a considerable amount of false fibers connections that give rise to false information especially when dealing with abnormal brain tissues.

The main objective of our project is to develop an algorithm that aims to improve the accuracy of the tractography results using fiber to bundle coherence measures by cleaning the tractography streamlines and getting rid of spurious fibers and thus obtaining more accurate 3d representation of the brain which will also improve tumors visualization.

Contents

List of figures

List of Tables

List of abbreviations

ADC ..... Apparent Diffusion Coefficient
CDA ..... Constant Solid Angle
CSD ..... Constrained Spherical Deconvolution
CST ..... Corticospinal Tract
dMRI ..... Diffusion Magnetic Resonance Imaging
DSI ..... Diffusion Spectrum Imaging
DT ..... Diffusion Tensor
DTI ..... Diffusion Tensor imaging
DW ..... Diffusion-Weighted
DWI ..... Diffusion Weighted Imaging
FA ..... Fractional Anisotropy
FBC ..... Fiber to Bundle Coherence
fMRI ..... Functional MRI
FOD ..... Fiber Orientation Distribution
FRT ..... Funk-Radon transform
GFA ..... General Fractional Anisotropy
GM ..... Gray Matter
HARDI ..... High Angular Resolution Diffusion Imaging
KDE ..... Kernel Density Estimation
LFBC ..... Local FBC
LUT ..... LookUp Table
MD ..... Mean diffusivity
MRI ..... Magnetic Resonance Imaging
ODF ..... Orientation Distribution Function
QSI ..... Q-space Imaging
RF ..... Radio Frequency
RFBC ..... Relative FBC
RK ..... Runge-Kutta
ROI ..... Region Of Interest
uODF ..... Uncertainty Orientation Density Function
WM ..... White Matter

GENERAL INTRODUCTION

General Introduction

Cerebral dissection used to be the only way to access the neural, then anatomists started using chemical markers to do neurography. More recently, neural fiber tractography based on local injection of chemical markers and subsequent observation of the induced propagation yielded high-quality connectivity mapping in the cat and monkey cerebral cortex. As of today, diffusion-weighted (DW) magnetic resonance imaging (MRI) is the unique noninvasive technique capable of quantifying the anisotropic diffusion of water molecules in biological tissues like the human brain white matter.

The great success of DW-MRI comes from its capability to accurately describe the geometry of the underlying microstructure. DW-MRI captures the average diffusion of water molecules, which probes the structure of the biological tissue at scales much smaller than the imaging resolution. The diffusion of water molecules is Brownian under normal unhindered conditions, but in fibrous structure such as white matter, water molecules tend to diffuse along fibers. Due to this physical phenomenon, DW-MRI is able to obtain information about the neural architecture in vivo.

On the other side, tractography has opened an entirely new noninvasive window on the white matter connectivity of the human brain and allows to visualize the different fibers connections.

The connections of fibers in the human brain are complicated, and a crucial limitation of tractography is its inability to determine the precise origin and termination of fibers connections and usually ends up with many false fibers' connections.

One of the major challenges of the tractography is to get precise connections and get rid of the spurious neural connections, that's why we are presenting in this work a method to improve the accuracy of the tractography output.

The starting point and motivation of this work is to overcome the limitations of the tractography process by Cleaning its results and eliminate the spurious fibers that give rise to unprecise fibers connections, that would result in more precise visualization of tumors in brains with abnormal tissues.

This report consists of four chapters. The **first chapter** aims to give an overall overview of the brain anatomy and it neural tissues and to present some MRI basics and principles and covers the principles of DW-MRI and high angular resolution diffusion imaging (HARDI)

reconstruction techniques. In particular, the fiber reconstruction algorithms to infer microstructure of biological tissues. The **second chapter** is devoted for presenting tractography algorithms both deterministic and probabilistic and showing the difference between them and then we will show our contribution by improving the tractography process by cleaning the results based on the bundle to fiber measures. Ultimately, **chapter three** presents the experimental results obtained from applying the algorithms described in chapter two and three on our dataset. Finally, we present our conclusions about the experiments and the results and suggest possible perspectives are drawn.

CHAPTER I

Brain Anatomy, MRI Basics and Reconstruction Methods

I.1 Introduction

In this chapter, we will start by covering the basic cerebral anatomy of the white matter. In particular, what are the different brain and neural tissues? What is the organization of the white matter? How is the brain connected? What are some of the large fiber bundles in the brain? And cover some MRI basics and how it works. These notions are important to understand

Afterwards, we will cover different reconstruction methods end their evolution from basic diffusion principles and diffusion tensor imaging to q-space imaging (QSI), high angular resolution diffusion imaging (HARDI) and beyond.

I.2. The human brain and neural tissue

The brain can roughly be split up into two different tissue types: gray matter and white matter. The gray matter (GM) contains neuronal cell bodies and dendrites, and can be found in the cerebral cortex and basal nuclei. Moreover, gray matter is predominantly found in the functional regions of the brain, such as the sensory, motor and association areas. White matter (WM) mainly consists of myelinated fibers, the axons, that are grouped into WM bundles/tracts. Specifically, the WM bundles form the connections that allow the different functional regions of the brain to communicate with each other and the rest of the body.

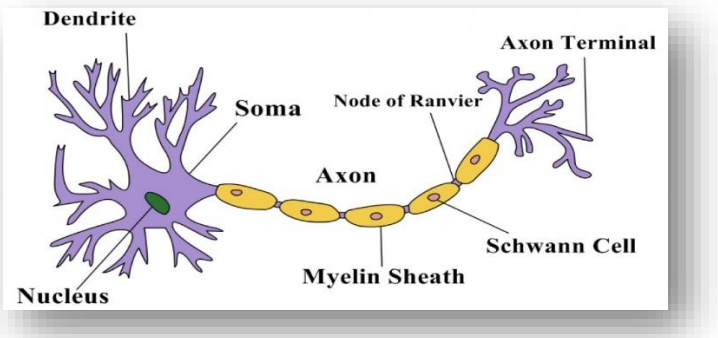

Figure I.1: *Structure of a typical neuron [1].*

I.3. Diffusion in the brain

At a microscopic scale, water molecules freely move and collide with each other in an isotropic medium according to Brownian motion [1]. This is illustrated in Figure I.2.

The macroscopic process of diffusion can also be described by Fick's first law, derived by Adolf Fick in 1855 [2]. It relates the concentration difference of the diffusion substance C to a flux. The flux, J, is proportional to the gradient of the concentration, ∇C. The

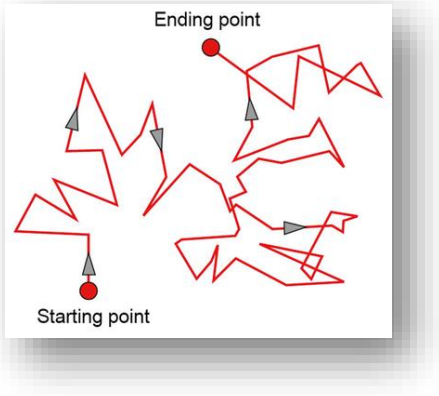

Figure I.2: *Simulation of Brownian motion of a particle.*

proportionality constant D is the diffusion coefficient and the governing equation is given by

$$J = -D\nabla C \tag{I.1}$$

However, the Brownian motion is not efficient when it comes to detecting single water molecules as opposed to detecting a large set of particles.

The diffusion probability density function was related by Einstein which is able to predict the displacement given a period of time. [3]

$$p(r,t) = \frac{1}{\sqrt{(4\pi t d_c)^3}} e^{\frac{-\|r\|^2}{4td_c}} \tag{I.2}$$

*Where: $\boldsymbol{d_c}$ is the diffusion coefficient (unit: m^2/s), **r** is the displacement vector (unit: m), **t** is the time (unit: s).*

From equation (I.2), we can derive Einstein's equation that describes the relation between the mean squared displacement and the diffusion coefficient

$$\|r\|^2 = 6d_c t \tag{I.3}$$

Importantly, isotropic diffusion occurs when the motion of the molecules is equal in all directions, whereas a directionally dependent diffusion is referred to as anisotropic diffusion. In the brain, anisotropic diffusion primarily occurs in the white matter, whereas the diffusion in gray matter is mostly isotropic.

I.4. MRI Basics

In magnetic resonance imaging (MRI), magnetic fields are used to manipulate and measure the magnetization due to nuclear spins in the body. In order to create an image, three types of magnetic fields are used in MRI. First of all, the nuclear spins are aligned in the direction of a strong static magnetic field (> 1.5 Tesla), the B_0 field. The nuclear spins (and therefore the magnetization) will start to precess around this B_0 field at a frequency known as the Larmor frequency, which is proportional to the field strength.

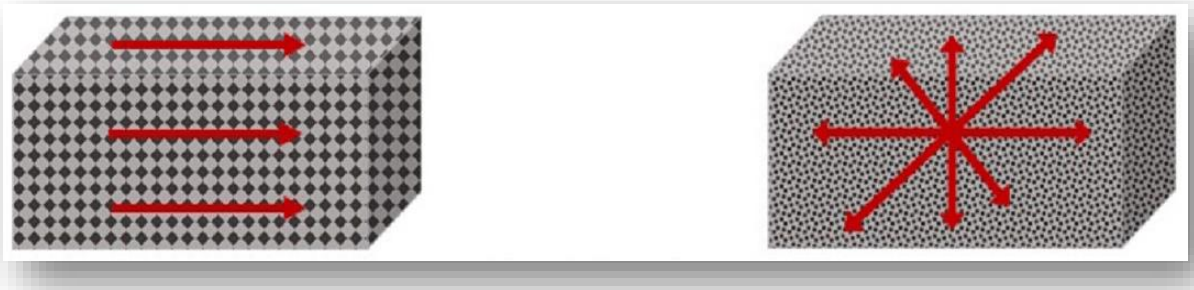

Figure I.3: *a)- Anisotropic layered structure* *b)- Isotropic uniform structure*

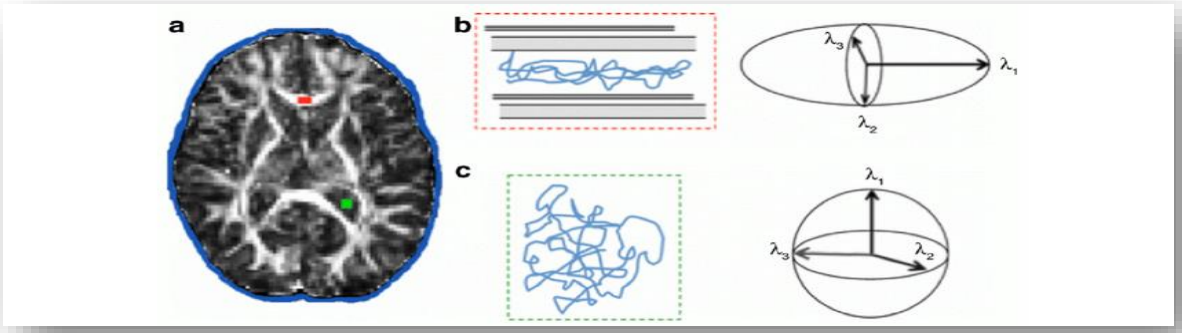

Figure I.4: *Figure: Isotropic and anisotropic diffusion in the brain. In the white matter of the corpus callosum (red), diffusion occurs preferentially along the axonal fibers, resulting in anisotropic diffusion (b). In the ventricular cerebrospinal fluid (CSF; green), diffusion is unhindered and can be described as isotropic (c). Diffusion tensor ellipsoids representing anisotropic and isotropic diffusion are shown in b and c, respectively.*

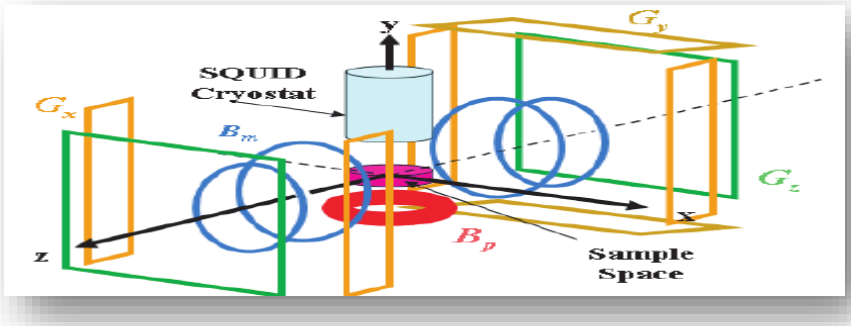

Figure I.5: *Schematic of the MagViz system. One pair of G y gradient coils is not shown for clarity.*

Seven Gradient coils are used to generate gradients in the static magnetic field and introduce a positional dependency of the precession frequencies, which makes it possible to differentiate between signals coming from different positions in the body. Lastly, radio frequency (RF) fields are used to flip the magnetization into a plane that is transverse to the B_0 field. This allows for measurement of the weak RF fields generated by the processing spins using receive coils. As a result of the positional dependence of the precession frequency this signal can be used to form an image

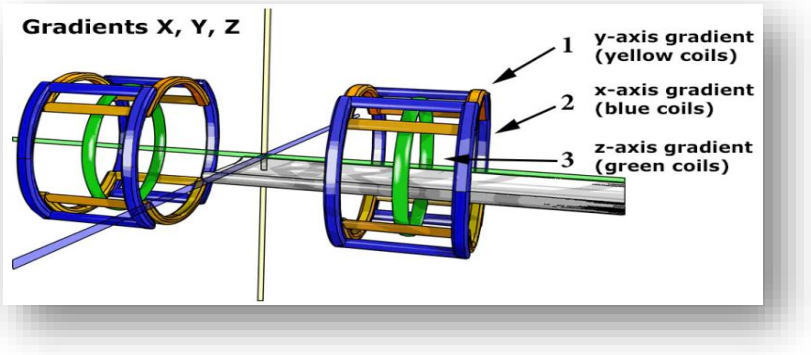

Figure I.6: *Gradients components.*

I.4.1. Pulse gradient spin echo

The Stejskal-Tanner imaging sequence is used to measure the diffusion of water molecules in a given direction g_i , i = 1,...,N. This pulse sequence is illustrated in Figure I.7. This sequence uses two gradient pulses g(t) in the direction g, of duration time δ, to control the diffusion-weighting. They are placed before and after a 180°, degrees refocusing pulse. More specifically, a first 90° degrees RF is applied to flip the magnetization in the transverse plane. The first gradient pulse causes a phase shift of the spins whose position are now a function of time. Spin position is in fact assumed to stay constant during time δ. Finally, the 180° pulse combined with the second gradient pulse induces another phase shift. It is applied after a time Δ separating the two gradient pulses. This pulse cancels the first phase shift only for static spins. On the other hand, spins under Brownian motion during the time period Δ separating the two pulses undergo different phase shifts by the two gradient pulses, resulting in a T2 signal attenuation [4].

Stejskal and Tanner [5] showed that the signal attenuation S(q,τ) is expressed as the 3-dimensional (3D) Fourier transform F of the ensemble average propagator P,

$$\frac{S(q,\tau)}{S_0} = \int_{\Re^3} P(r|r_0,\tau)e^{-2\pi i q^T R}dr = F[P(r|r_0,\tau)] \quad \text{(I.4)}$$

Where the value of ***q*** *is given by* ***q*** *=* $\boldsymbol{\gamma\delta G/2\pi}$*, with* $\boldsymbol{\gamma}$ *the nuclear gyromagnetic ratio for water protons,* ***G*** *the applied diffusion gradient vector,* $\boldsymbol{S_0}$ *is the baseline image acquired without any diffusion gradients (also called b = 0 image) and* $\boldsymbol{P(r|r_0,\tau)}$ *is the diffusion PDF or diffusion propagator of water molecules introduced earlier. This* ***P*** *is ultimately the function we are looking to reconstruct in diffusion MRI.*

Intuitively, one has to sample the diffusion PDF along many q vectors to be able to reconstruct the diffusion PDF. The space of all possible 3D q vectors is called q-space. This is

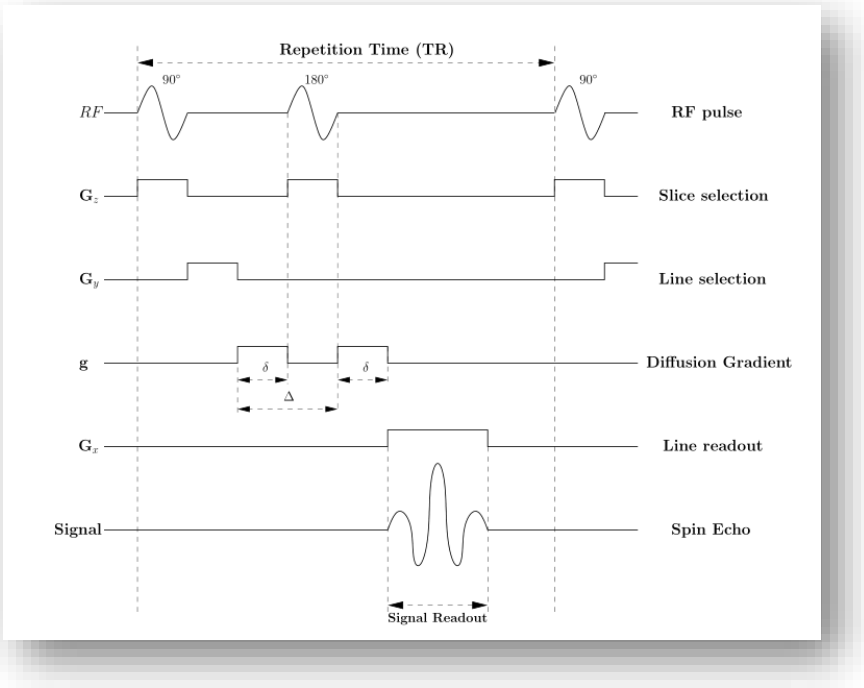

Figure I.7: *Schematic Stejskal-Tanner imaging PGSE sequence. RF pulses could more realistic.*

the idea behind q-space imaging [6]. If the diffusion PDF is assumed to be Gaussian, one can work out the Fourier integral in Eq. I.4 analytically. The Stejskal-Tanner signal attenuation equation then becomes:

$$S(q,\tau) = S_0 e^{-rq^T Dq} \quad \text{(I.5)}$$

Where $D(q) = q^T Dq$ is the ADC. The signal attenuation is also often written with respect to unit vector, $g = q/|q|$, and it is common to introduce the b-value, $b = \tau|q|^2$. We thus obtain a signal attenuation with respect to the b-value given by

$$S(q,\tau) = S_0 e^{-\tau|q^2|g^T Dg} \leftrightarrow S(b,g) = S_0 e^{-bg^T Dg} = S_0 e^{-bg^T Dg} \quad \text{(I.6)}$$

I.4.2. Diffusion-Weighted Imaging (DWI) and b-values

Diffusion-weighted imaging (DWI) is a form of MR imaging based upon measuring the random Brownian motion of water molecules within a voxel of tissue. In general, simplified terms, highly cellular tissues or those with cellular swelling exhibit lower diffusion coefficients. Diffusion is particularly useful in tumor characterization and cerebral ischemia. The diffusion is restricted by the structure of the tissue and this is normally called the apparent diffusion coefficient (ADC). The MR signal in dMRI is proportional to the T_2 relaxation, the diffusion in a voxel and the intra-voxel in-coherent motion. These last two parameters cannot be measured independently and are combined in the apparent diffusion coefficient (ADC), which results in the signal equation given below:

$$S = [\rho] e^{\frac{-t}{T_2}} e^{-bD} \tag{I.7}$$

Equation I.7 shows that the signal measured in dMRI is proportional to the proton density [ρ] and can be seen as a mix of a T_2 weighted signal and a diffusion weighted signal. The b-value is a factor that reflects the strength and timing of the gradients used to generate diffusion-weighted images. The higher the b-value the stronger the diffusion effects. Figure I.8 shows DW images for different b-values. We clearly note the importance of the b-value.

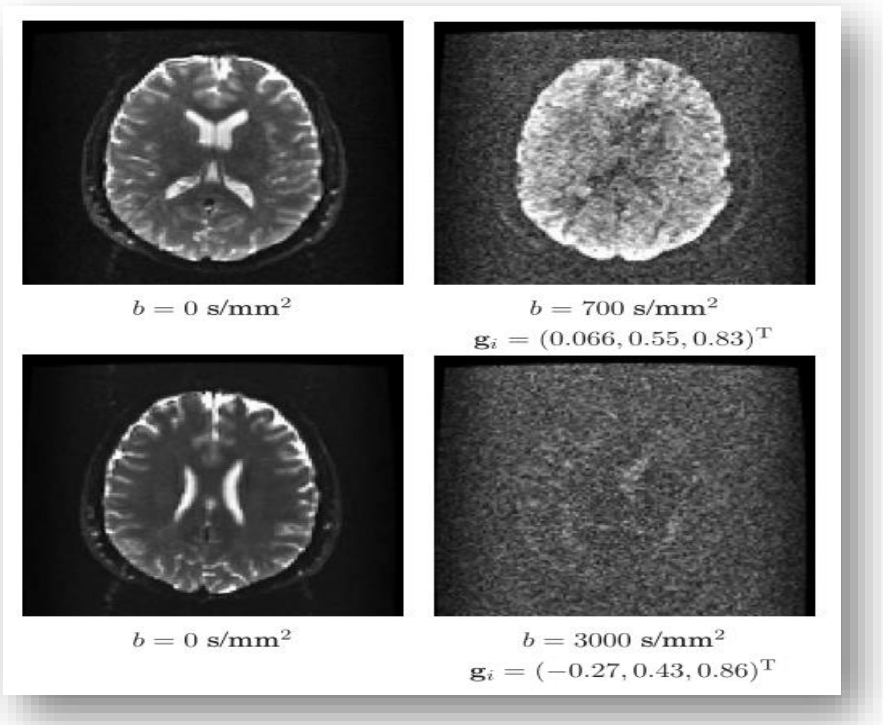

Figure I.8: *Diffusion-weighted images for different b-values.*

The b-value is a function of the parameters shaping the gradient pulses, has units of $mm^{-2}s$ and is defined as:

$$b = \gamma^2 G^2 \delta^2 (\Delta - \frac{\delta}{3}) \quad \text{(I.8)}$$

Where γ represents the gyromagnetic ratio, G denotes the strength of the diffusion sensitizing gradient pulses, δ is the duration of the separate pulse sand Δ stands for the time between the starting points of the two pulses

I.5 Reconstruction techniques:

One of the main goals of modern diffusion MRI is to determine, from a set of measurements in each voxel of an image volume, the dominant fiber orientation(s) in each voxel. Diffusion-tensor MRI was the first method to allow mapping of fiber orientations over an image volume and remains the most common. However, a drawback of diffusion-tensor MRI is that it can only reveal a single fiber orientation in each voxel and fails in voxels containing complex tissue architecture with more than one significant fiber orientation. Recently, a new generation of diffusion MRI technique has emerged. These techniques retain the desirable qualities of both diffusion-tensor MRI and aim to reveal complex tissue architectures with acquisition requirements similar to diffusion-tensor MRI.

I.5.1. Diffusion Tensor Imaging (DTI)

A. Diffusion Tensor model

In vivo, the exponential proportionality of the dMRI signal to a single scalar ADC is only true in tissue with isotropic diffusion. If we want to describe anisotropic diffusion, the 3D diffusion profile needs to be taken into account. The diffusion tensor (DT) models the diffusion profile as an ellipsoid by assuming a single Gaussian diffusion process in a voxel, which is described by a 3 x 3 DT [40]:

$$D = \begin{bmatrix} D_{xx} & D_{xy} & D_{xz} \\ D_{yx} & D_{yy} & D_{yz} \\ D_{zx} & D_{zy} & D_{zz} \end{bmatrix} \quad \text{(II.9)}$$

With the diagonal elements representing the diffusion in three orthogonal directions and the off-diagonal elements representing the correlations of random motion between each pair of principal direction. In general, the orthogonal directions (x,y,z) are aligned with the gradients of the MR-system. The DT can be estimated by solving a linear system of 7 acquisitions, which consist of 6 acquisitions with non-colinear gradient directions and a b=0 acquisition to estimate the non-diffusion weighted signal.

The diffusion tensor is represented in 3×3 symmetric matrix as shown in figure I.9, where $D_{XY} = D_{YX}$, $D_{XZ} = D_{ZX}$ and $D_{YZ} = D_{ZY}$. This means the diffusion tensor matrix is symmetric with only 6 unique elements. To estimate all of them we need a minimum of 7 measurements, one baseline (b0) and 6 source data sets.

The diffusion tensor is usually calculated from diffusion weighted images (DWI) by solving the Stejskal-Tanner equation:

$$S_k = S_0 e^{-b g_k^T D g_k} \tag{I.10}$$

Where g is the gradient direction is written as:

$$g = \begin{pmatrix} g_x \\ g_y \\ g_z \end{pmatrix} \tag{I.11}$$

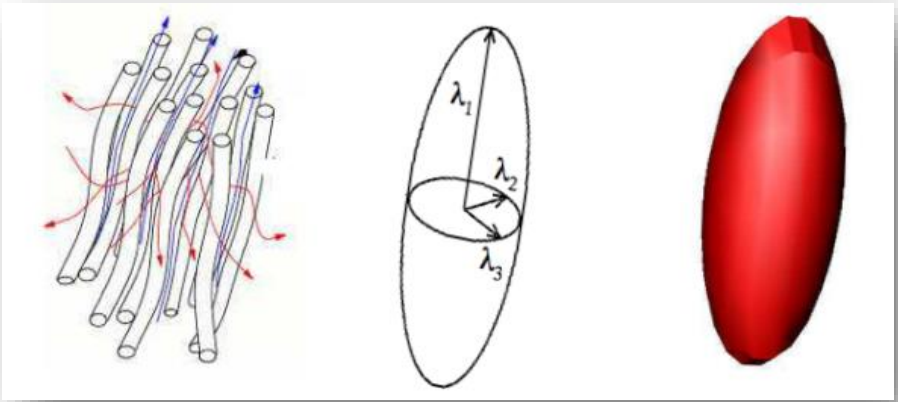

Figure I.9: *Diffusion tensor representation*

From Eq. (I.10) we get:

$$g^T D g = -\frac{\ln(\frac{S}{S_0})}{b} \tag{I.12}$$

By replacing g and D in Eq. (I.12) we get:

$$(g_x \quad g_y \quad g_z)\begin{pmatrix} D_{xx} & D_{xy} & D_{xz} \\ D_{yx} & D_{yy} & D_{yz} \\ D_{zx} & D_{zy} & D_{zz} \end{pmatrix}\begin{pmatrix} g_x \\ g_y \\ g_z \end{pmatrix} = -\frac{\ln(\frac{S}{S_0})}{b} \tag{I.13}$$

The right side of Eq. (I.13) can be expanded as follows:

$$g^T D g = g_x^2 D_{xx} + g_y^2 D_{yy} + g_z^2 D_{zz} + 2 g_x g_y D_{xy} + 2 g_x g_z D_{xz} + 2 g_y g_z D_{yz} \tag{I.14}$$

We replace now the Eq. (I.13) in Eq. (I.14) equation we get:

$$g_x^2 D_{xx} + g_y^2 D_{yy} + g_z^2 D_{zz} + 2g_x g_y D_{xy} + 2g_x g_z D_{xz} + 2g_y g_z D_{yz} = -\frac{\ln(\frac{S}{S_0})}{b} \quad \text{(I.15)}$$

S_k, S_0, g_k are all known, and Since we have six unknown parameters of the diffusion tensor we need M applied gradient where M > 6.

Finally, we get

$$g_i^T D g_i = -\frac{\ln(\frac{S}{S_0})}{b} \qquad i \in 1, \ldots, M \quad \text{(I.16)}$$

$$\begin{pmatrix} g_{1,x}^2 & g_{1,y}^2 & g_{1,z}^2 & 2g_{1,x}g_{1,y} & 2g_{1,x}g_{1,z} & 2g_{1,y}g_{1,z} \\ .. & .. & .. & .. & .. & .. \\ g_{M,x}^2 & g_{M,y}^2 & g_{M,z}^2 & 2g_{M,x}g_{M,y} & 2g_{M,x}g_{M,z} & 2g_{M,y}g_{M,z} \end{pmatrix} \begin{pmatrix} D_{xx} \\ D_{yy} \\ D_{zz} \\ D_{xy} \\ D_{xz} \\ D_{yz} \end{pmatrix} = \frac{-1}{b_i} \begin{pmatrix} \ln(\frac{S_1}{S_0}) \\ . \\ . \\ . \\ \ln(\frac{S_M}{S_0}) \end{pmatrix} \quad \text{(I.17)}$$

To solve for diffusion tensor parameters, we apply the Linear Least Square method wich is illustrated in Eq. (I.18) on Eq. I.17):

$$x^* = (A^T A)^{-1} A^T Y \quad \text{(I.18)}$$

Where

$$x^* = \begin{pmatrix} D_{xx} \\ D_{yy} \\ D_{zz} \\ D_{xy} \\ D_{xz} \\ D_{yz} \end{pmatrix} \quad \text{(I.19)}$$

$$A = \begin{pmatrix} g_{1,x}^2 & g_{1,y}^2 & g_{1,z}^2 & 2g_{1,x}g_{1,y} & 2g_{1,x}g_{1,z} & 2g_{1,y}g_{1,z} \\ .. & .. & .. & .. & .. & .. \\ g_{M,x}^2 & g_{M,y}^2 & g_{M,z}^2 & 2g_{M,x}g_{M,y} & 2g_{M,x}g_{M,z} & 2g_{M,y}g_{M,z} \end{pmatrix} \quad \text{(I.20)}$$

$$Y = \frac{-1}{b_i} \begin{pmatrix} \ln(\frac{S_1}{S_0}) \\ . \\ . \\ . \\ \ln(\frac{S_M}{S_0}) \end{pmatrix} \quad \text{(I.21)}$$

B. Diffusion Tensor Imaging measurements

The diffusion tension model allows us to extract many useful parameters, the main diffusion orientation is determined by finding the eigen vectors and the eigen values of the Diffusion Tensor. Other important properties can be computed such as the apparent diffusion coefficient (ADC) and the fractional anisotropy (FA) [41]. The diffusion matrix is symmetric and can be written as follows:

$$D = V\Lambda V^T = (e_1 \quad e_2 \quad e_3)\begin{pmatrix}\gamma_1 & 0 & 0\\ 0 & \gamma_2 & 0\\ 0 & 0 & \gamma_3\end{pmatrix}\begin{pmatrix}e_1\\ e_2\\ e_3\end{pmatrix} \tag{I.22}$$

Where

$$V = (e_1 \quad e_2 \quad e_3) \tag{I.23}$$

$$\Lambda = \begin{pmatrix}\gamma_1 & 0 & 0\\ 0 & \gamma_2 & 0\\ 0 & 0 & \gamma_3\end{pmatrix} \tag{I.24}$$

The eigenvectors and eigenvalues of the DT are used to probe the microstructure of tissue in a voxel. Particularly, the first eigenvector defines the orientation of the fiber bundles while the eigenvalues can be used to describe the microstructure using rotationally invariant measures such as the degree of anisotropy. (fractional anisotropy or FA) and mean diffusivity (MD). These are defined as:

$$FA = \sqrt{\frac{1}{2}}\frac{\sqrt{(\lambda_1 - \lambda_1)^2 + (\lambda_2 - \lambda_3)^2 + (\lambda_3 - \lambda_1)^2}}{\sqrt{\lambda_1^2 + \lambda_2^2 + \lambda_3^2}} \tag{I.25}$$

$$MD = \frac{\lambda_1 + \lambda_2 + \lambda_3}{3} \tag{I.26}$$

Where λ_i denotes the i^{th} eigenvector of the DT.

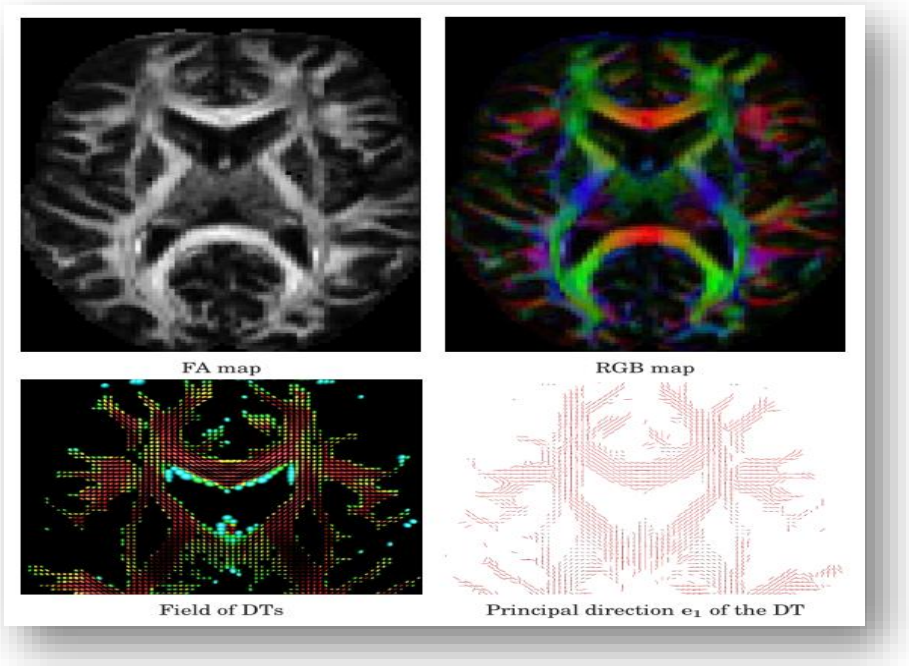

Figure I.10: *FA, RGB, field of diffusion tensors and principal diffusion direction of the DTs in an axial slice. The DTs are colored with respect to the FA map, blue to red corresponds to isotropic to anisotropic* tensors. The DTs and e 1 vectors are shown where FA > 0.1 in half the axial slice.

C. Limitations:

DTI and its assumption of a single Gaussian process has severe limitations as it is well known that the single tensor model does not hold in voxels with non-Gaussian diffusion. This is the case in voxels with multiple fiber populations, whose prevalence has been estimated to range from 33% up to ~90% of the WM voxels. Consequently, DTI based tractography leads to erroneously reconstructed WM pathways, and ambiguous correlations of the scalar measures. For example, in the case of two crossing fibers an increase in the FA of one fiber population will result in a decrease in the FA measured using DTI. This limitation of the DT model is illustrated in Figure I.11 for two orthogonally crossing fibers. The expected fiber distribution has two maxima whereas the reconstructed DT profile is planar-like with no preferred diffusion direction.

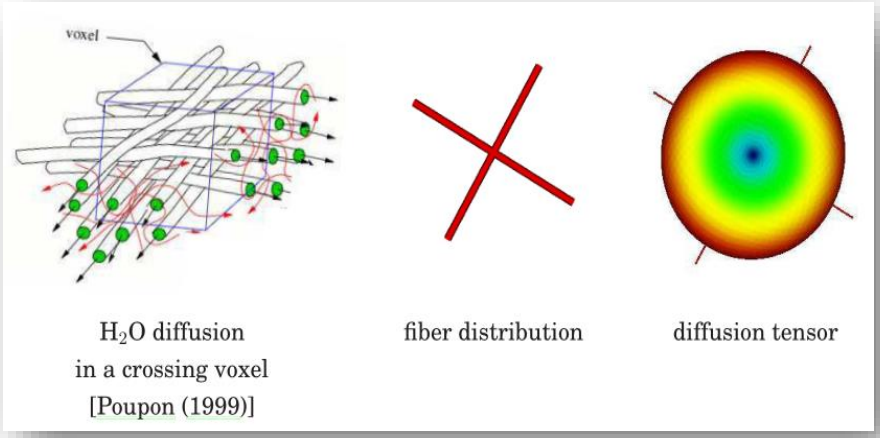

Figure I.11: *Limitation of DTI in voxels with crossing configurations. DTI cannot resolve imaging voxels containing multiple fiber crossings.*

I.5.2. High angular resolution diffusion imaging (HARDI) techniques

The goal of HARDI is to capture multiple fiber directions within the same imaging voxel. HARDI acquisitions are currently being improved every day with better material and better reconstruction algorithms. The idea now is to sample q-space along as many directions and q-magnitudes as possible in order to reconstruct the true diffusion PDF. This true diffusion PDF is model-free and can recover the diffusion of water molecules in any underlying fiber population. For example, Figure I.12 illustrates the expected diffusion PDF in the case of an isotropic imaging voxel, a single fiber imaging voxel and two crossing fibers imaging voxel. Note that we no longer have a scalar-valued or tensor-valued image but we now have a 3D image of 3D diffusion distributions. Hence, one can imagine that there are

technical requirements and trade-offs that one must make in HARDI acquisition. In particular, HARDI depends on the number of measurements N and the gradient strength (b-value), which will directly affect acquisition time and signal to noise ratio in the signal. Typically, there are two strategies used in HARDI: 1) sampling of the whole q-space 3D Cartesian grid or 2) single shell spherical sampling. In the first case, a large number of q-space points are taken over the discrete grid (N > 200) and the inverse Fourier transform of the measured DWI signal is taken to obtain an estimate of the diffusion PDF P. This is Diffusion Spectrum Imaging (DSI) in the HARDI literature and the theory of DSI goes back to the development of QSI by Callaghan [6], [7]. The method requires very strong imaging gradients ($500 \leq b \leq 20000$ s/mm^2) and a long time for acquisition depending on the number of sampling directions. The visualization of 3D diffusion PDF at every voxel is computationally intensive. Hence, people either take an isosurface of the diffusion PDF for a certain radius r or the diffusion orientation distribution function (ODF) is computed. The diffusion ODF contains the full angular information of the diffusion PDF and is defined as

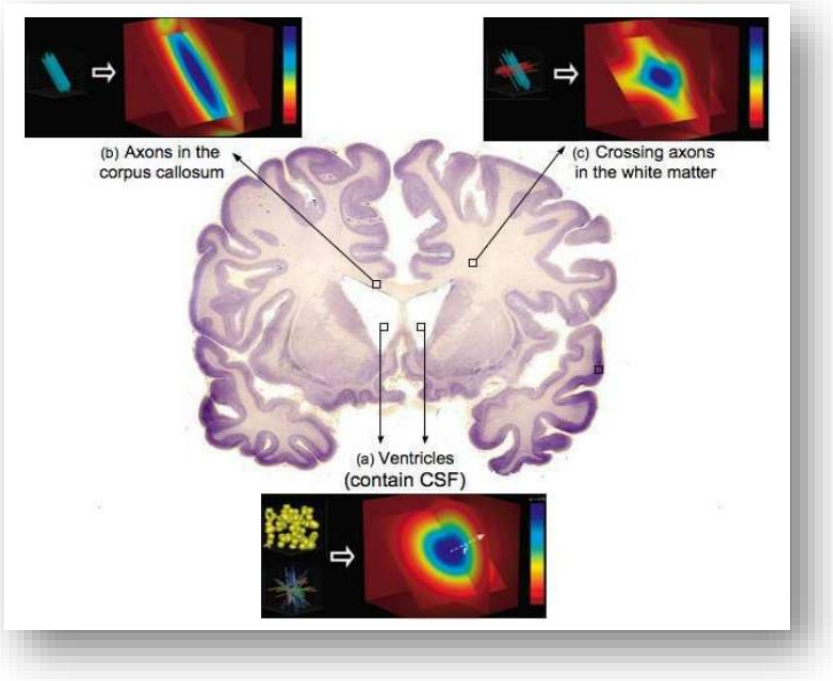

Figure I.12: *Expected diffusion PDF in isotropic, single fiber and two crossing fibers.*

$$\Psi(\theta,\varphi) = \int_0^{\infty} P(r,\theta,\varphi)dr \tag{I.27}$$

Where (θ, φ) obey physics convention in this project ($\theta \in [0, \pi]$, $\varphi \in [0, 2\pi]$). These data representations and data reductions for visualization are illustrated in Figure I.13. The diffusion ODF will play a central part of the project and is at the heart of Q-Ball Imaging (QBI).

In the second case, a discrete uniform sampling of the sphere is done for a certain radius in q-space (given by the b-value). The signal attenuation is thus measured on a single shell of q-space. The idea is that the radial information of the diffusion PDF can be discarded if one is interested in fiber directions. Thus, most single shell HARDI techniques aim at reconstructing the diffusion ODF or variants of this function in order to have a function whose maxima are aligned with the underlying fiber structure. More than 60 measurements are desirable and medium gradient strengths are acceptable although strong gradients give better diffusion ODF reconstructions. Typically, $60 \leq N \leq 200$, $b \geq 3000 s/mm^2$ is used and acquisition time is between 10 and 20 minutes.

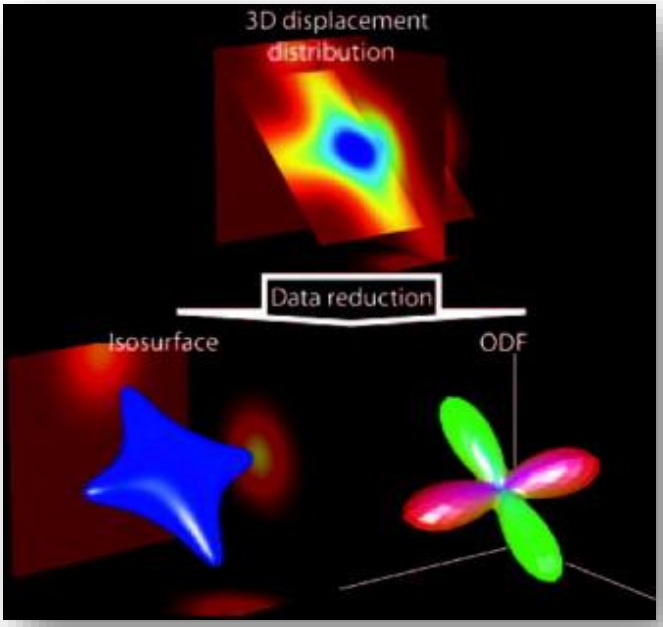

Figure I.13: *Simplifying visualization of the 3D diffusion PDF or 3D displacement distribution by either taking an isosurface of the distribution or computing the diffusion ODF. Image taken from [8].*

A. Diffusion Spectrum Imaging (DSI)

This technique suggests the fairly straightforward means of extracting the diffusion PDF from measurements in q-space by measuring the signal on a Cartesian grid of points in q-space and then taking the 3D inverse Fourier transform to obtain an approximated PDF. This technique is called q-space imaging (QSI) or diffusion spectrum imaging (DSI). However, DSI is restricted by severe technical limitations. First, in order to resolve features in the PDF of the order of some scale 1/a, it requires a box of side length > a in q-space. In practice, this requires many measurements and very large b-values compared to those used on conventional scanners. As we want δ small to satisfy the narrow pulse approximation, the gradients G must

be very high which creates eddy current distortions, and even can induce harmful electric fields in the subject. As a result of the DSI limitations, other techniques have been developed to attempt to extract the desired diffusion PDF and diffusion ODF information in a more efficient way. One such clinically feasible approach is single shell (HARDI) [9,10].

B. Q-Ball imaging

Tuch [10,11] showed that the diffusion ODF could be estimated directly from the raw HARDI measurements on a single sphere of q-space without computing the full diffusion PDF. The basic assumption of QBI is that angular information is enough to recover fiber orientation distributions (forgetting about radial information). Hence, QBI is a modality which takes advantage of the fact that significantly less information is required to construct an angular function in real space than is required to construct a volume function, as in DSI. Specifically, QBI seeks to reconstruct the diffusion ODF, a function defined in Eq. I.27, which is the radial projection of the diffusion PDF.

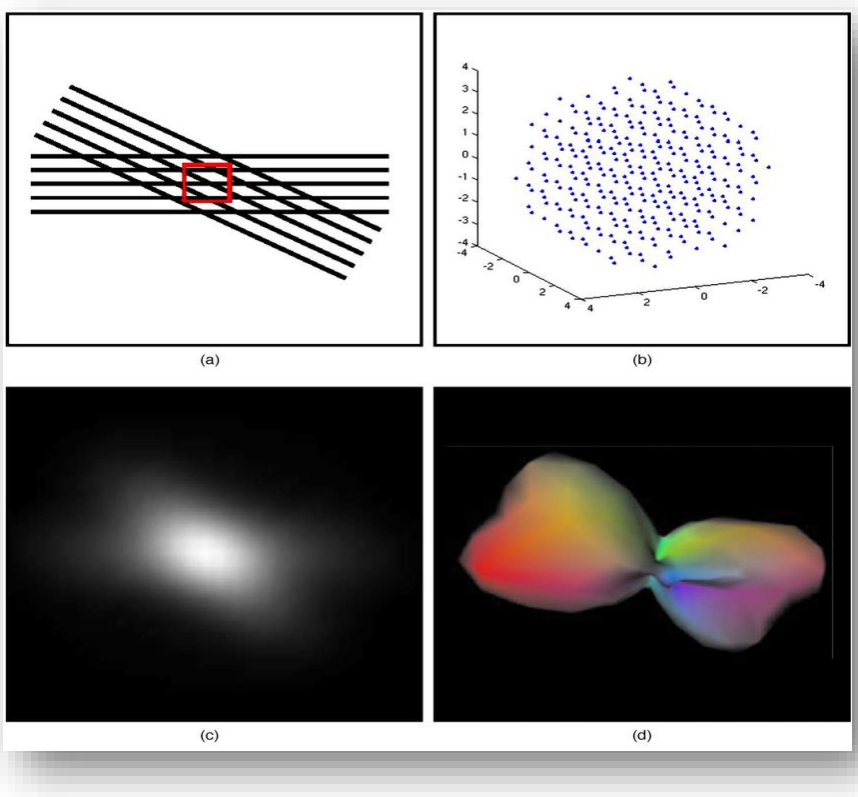

Figure I.14: *Derivation of fiber alignment from diffusion spectrum imaging*

To compute the ODF, the QBI modality uses the Funk-Radon transform (FRT) G, a transformation from the unit sphere to itself as illustrated in Figure I.15 In order to find the Funk-Radon transformed value of the signal on the sphere at a given point u, one needs to

first find the plane through the origin with normal vector u and then compute the one-dimensional integral over the intersection of that plane with the function on the original sphere. Intuitively, to find the new value at an arbitrarily defined "pole", one integrates the spherical function f over the corresponding "equator" or great circle. This can be written explicitly as

$$G[f(w)](u) = \int \delta(u^T w) f(w) dw \tag{I.28}$$

Where u and w are constrained to be unit vectors

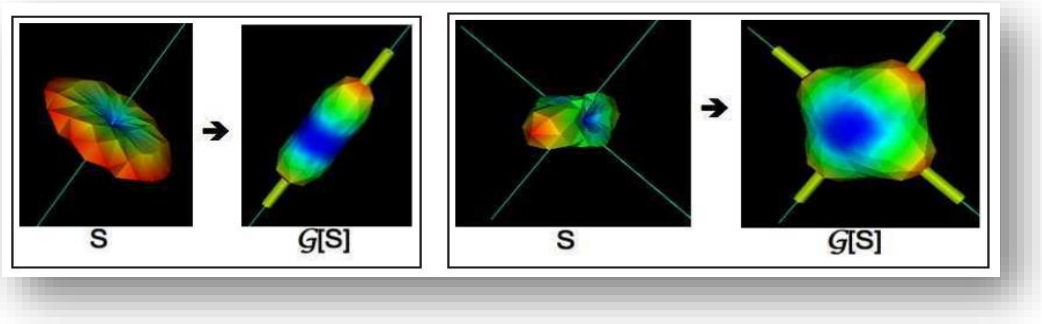

Figure I.15: *Funk-Radon Transform G[S] illustrated for the HARDI signal S with 1 fiber (left) and two orthogonal fibers (right). The thin lines are the true underlying fiber orientations and the thicker tubes are the detected maxima. These functions are spherical functions and for visualization purposes, the radius of the respective spheres are scaled by the corresponding value on the surface.*

C. The Spherical Harmonics

Some of the reconstruction methods make use of spherical harmonics modeling to represent functions on the sphere, we begin with an introduction to spherical harmonics. Spherical harmonics Y_l^m of order l and degree m are the angular portion of Laplace's equation in spherical coordinates. They are defined as:

$$Y_l^m(\theta, \varphi) = \sqrt{\frac{(2l+1)(l-m)!}{4\pi(l+m)!}} P_l^m(cos\theta) e^{im\varphi} \tag{I.29}$$

In order to have an idea of what spherical harmonics look like, we show in Figure I.16 the real part squared, $\mathrm{Re}[Y_l^m(\theta, \varphi)]^2$, of the spherical harmonics Y_l^m up to order 3.

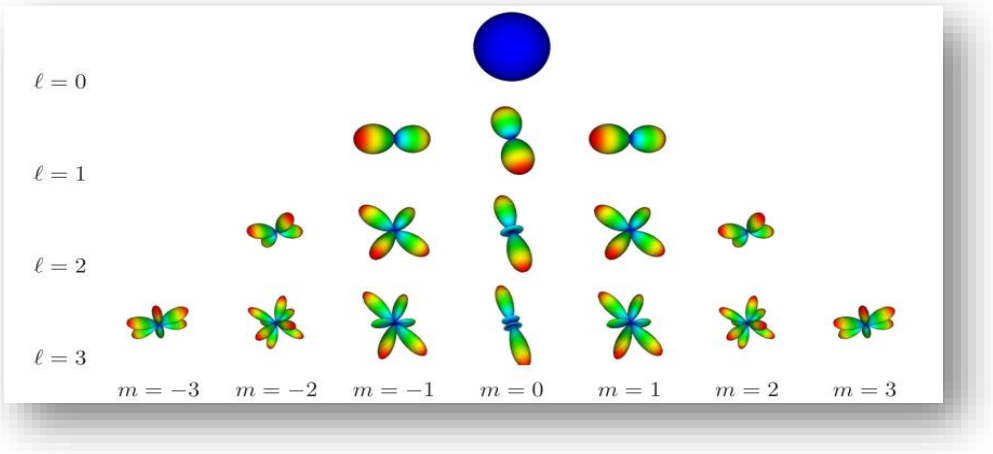

Figure I.16: Real part squared $\mathrm{Re}[Y_l^m(\theta,\varphi)]^2$ of the spherical harmonics basis up to order 3.

D. The Modified Real Spherical Harmonics Basis

The spherical harmonics Y_l^m (Eq. I.29) are a basis for complex functions on the unit sphere. Hence, any complex function defined on the sphere can be expressed as a series of spherical harmonics. This is very powerful and analogous to the Fourier transform very often used in image processing. In that case, any image can be decomposed in a Fourier series, namely in a sum of sinusoids and cosines. In this project, we have physical diffusion MRI measurements that represent the average attenuation of the diffusion of water molecules. Hence, the HARDI signal is assumed to be real and symmetric. Therefore, we want to define a modified spherical harmonic basis that is also real and symmetric.

For $l = 0,2,4,\ldots,L$ and $m = -l,\ldots,0,\ldots,l$, we define a single index j in terms of l and m such that $j(l,m) = \frac{(l^2+l+2)}{2+m}$. The modified basis then is

$$Y_j = \begin{cases} \sqrt{2}Re\left(Y_l^{|m|}\right), & if\ m < 0 \\ Y_l^{|m|}, & if\ m = 0 \\ \sqrt{2}(-1)^{m+1}Im\left(Y_l^{|m|}\right), & if\ m < 0 \end{cases} \quad \text{(I.30)}$$

Where $Re\left(Y_l^{|m|}\right)$ and $Im\left(Y_l^{|m|}\right)$ represent the real and imaginary parts of Y_l^m respectively.

Figure I.17 shows the spherical harmonics in the modified basis of order 4, L = 4.

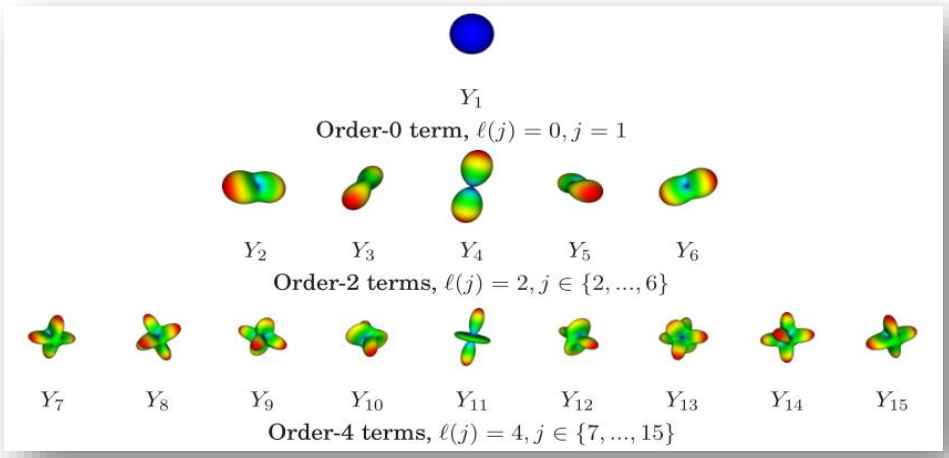

Figure I.17: *Modified spherical harmonics up to order L = 4. l(j) represents the harmonic order for the j^{th} coefficient.*

E. Spherical Deconvolution

Spherical deconvolution was introduced approximately at the same period as q-ball imaging. Spherical convolution assumes that a distribution of fiber orientations convoluted with a single-fiber response function generates the measured diffusion signal, as illustrated in Figure I.19. Hence, the idea is to view the HARDI signal S as the convolution of the response function produced by a single-fiber R with the expected true fiber orientation distribution F. The problem can also be viewed more intuitively in real space using the ODF. The signal or ODF response function used as the deconvolution kernel is normally estimated from the data itself. Typically, we can use the corpus callosum voxels or voxels with a FA above 0.7 to estimate the response function R there. Alternatively, it can also be directly modeled with an appropriate signal or ODF for a single fiber. Then, using spherical harmonics theory and the convolution theorem, the problem is defined as a multiplication in spherical harmonics space: $S = R \cdot F$. Hence, using a least-squares formulation, one can solve for the FOD: $F = (R^T R)^{-1} S$. Hence, spherical deconvolution cannot be considered as a model-free technique because it needs a deconvolution kernel. In a sense, it is at the frontiers of model-free and model-based techniques. However, the linear solution just described of spherical deconvolution suffers from severe instabilities at high harmonic orders that lead to negative fiber ODF values and false spurious peaks. Hence, the original spherical deconvolution method was improved using nonlinear methods to better deal with the instabilities, noise, and negative diffusivities appearing in the deconvolution process.

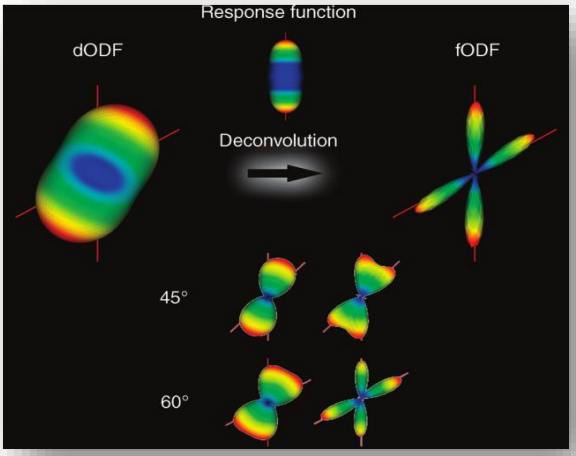

Figure I.18: *Spherical deconvolution intuition to improve angular resolution of ODF reconstruction. Assuming a particular response function, the deconvolution will remove the "blurry" part of the diffusion ODF to obtain a sharp fiber ODF that better captures the underlying fiber populations. Hence, a better angular resolution can be obtained, as illustrated in 45 + and 60 + crossing in the bottom of the figure.*

The measured signal S can be evaluated according to the following equation

$$S(\theta, \varphi) = F(\theta, \varphi) \circledast R(\theta) \tag{I.31}$$

Where S is the measured signal, F is the fODF an R is the fiber response. Hence the problem of estimating the fiber orientations themselves is solved by inverting the problem to infer the FODF from the measured signal.

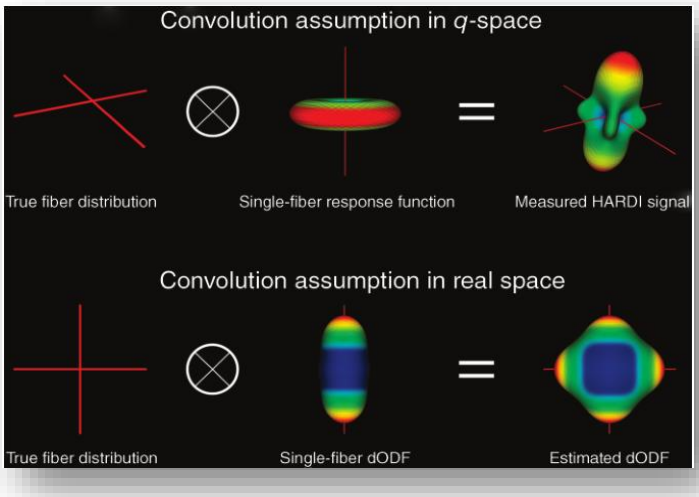

Figure I.19: *Spherical deconvolution techniques. Convolution assumption in q-space (signal space) and real space (ODF space). Deconvolution techniques seek tore construct the true fiber orientation distribution (FOD) or fiber orientation distribution function (fiber ODF) from an assumed single-fiber response function.*

I.6. Summary:

In this chapter we have seen an overall overview about the brain anatomy and its neural tissues. We presented also some MRI basics and its functionality and some basic principles were introduced for a better understanding of the physics behind the magnetic resonance imaging. Then, we explained how weighted imaging works and its relation with water diffusivity and b-values.

Next, we saw the evolution of diffusion MRI from simple scalar DWI, to tensor DWI or DTI and beyond to HARDI techniques able to recover the 3D diffusion PDF and diffusion ODF of water molecules in biological tissues. In this project, we focus on techniques beyond the diffusion tensor imaging because they are able to recover complex multiple fiber distributions. We also saw the solution that each technique proposed to overcome the problem of multifiber detection of DTI.

CHAPTER II

Fiber Tracking and Proposed Post-Processing

II.1. Introduction

Fiber tractography pieces together the local WM orientations to infer long-range connectivity patterns between distant brain regions. Diffusion MRI based fiber tractography is unique in its ability to delineate the WM fiber pathways in a non-invasive way. This raises possibilities for clinical applications and can provide new insights in neuroscientific research.

Fiber tractography algorithms can be classified largely into deterministic, probabilistic, and global algorithms. In this chapter, we will discuss these different approaches and their limitations. We end the chapter with a brief overview of the current application.

II.2. Deterministic tractography

Deterministic streamline tractography is currently the most common method for fiber tractography [12]. A streamline through a vector field is any line whose tangent is parallel to the local vector during its entire course. Mathematically, a line can be represented as a 3D space curve $r(s)$, parameterized by its arc length s. In order for a streamline to align with the vector field, the tangent at arc length s , has to be equal to the vector at the corresponding position:

$$\frac{dr(s)}{ds} = v[r(s)] \tag{II.1}$$

Where $r(s)$ denotes the 3D position along the streamline and v is the 3D vector field.

Note that Eq. (II.1) is a differential equation that can be solved by means of integration:

$$r(s) = \int_{s_0} v[r(s)] \tag{II.2}$$

Where $r(s_0) = r_0$ represents the starting point of the streamline which is often referred to as seed point. Formally, streamline tractography can be defined as the process of integrating voxelwise fiber orientations into fiber pathways.

A. Integration

The most intuitive way to perform the numerical integration of Eq. (II.2) is by starting the procedure at seed point r_0, calculating the corresponding fiber orientation $v(r_0)$, and following that direction for a short distance Δ, which is called the 'step size', to obtain the next point $r_1 = r_0 + v(r_0)\Delta$ on the pathway. This method, known as Euler integration, can reconstruct the entire streamline by iteratively performing this procedure:

$$r_{i+1} = r_i + \mathrm{v}(r_i)\Delta \tag{II.3}$$

Note that Eq. (II.3) assumes that the value r_i is constant during the step size Δ, which will make this method susceptible to overshoot in highly curved regions, especially for larger step sizes (Figure II.2). In order to take into account the variations of v between r_i and r_{i+1}, the use of higher order numerical integration schemes has been proposed, such as the second-order Runge-Kutta (RK2) or midpoint integration scheme:

$$r_{i+1} = r_i + \mathrm{v}(r_i + \mathrm{v}(r_i)\frac{\Delta}{2})\Delta \tag{II.4}$$

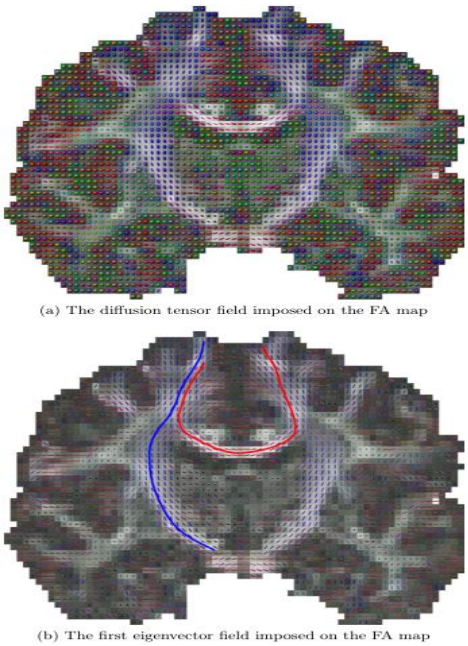

(a) The diffusion tensor field imposed on the FA map

(b) The first eigenvector field imposed on the FA map

Figure II.1: *Example of DTI streamlines on coronal slices of the human brain. The blue streamline corresponds to the corticospinal tract (CST). The red streamline corresponds to the corpus callosum. Note that each streamline's tangent is parallel to the local vector field during its entire course*

Which has an associated error of order $O(\Delta^3)$ or the fourth-order Runge-Kutta (RK4) scheme

$$r_{i+1} = r_i + \frac{k_1}{6} + \frac{k_2}{3} + \frac{k_3}{3} + \frac{k_4}{6} \tag{II.5}$$

With

$$k_1 = \mathrm{v}(r_i)\Delta \tag{II.6}$$

$$k_2 = \mathrm{v}(r_i + \frac{k_1}{2})\Delta \tag{II.7}$$

$$k_3 = \mathrm{v}(r_i + \frac{k_2}{2})\Delta \tag{II.8}$$

$$k_2 = \mathrm{v}(r_i + k_3)\Delta \tag{II.9}$$

The RK4 scheme has an associated error of order $O(\Delta^5)$ and is known to be a good candidate for the numerical solution of Eq. (II.2).

B. Interpolation

The simplest method to obtain an estimate of the local fiber orientation at any location is to use nearest-neighbor interpolation [13,14]. This method approximates the desired fiber orientation by that of the nearest voxel. However, this approach leads to a much greater propagation of errors than approaches that perform a smooth interpolation between grid points (Figure II.3) [15]. Smooth interpolation methods assume that the fiber orientations between grid points contain contributions from each neighboring point. Most algorithms use trilinear interpolation, where the quantity of interest is calculated as a weighted sum from the 8 voxels nearest to the point of interest with the weight of each neighboring voxel determined by their distance to the point of interest. Some implementations perform trilinear interpolation on the raw diffusion weighted data and recompute the DT/dODF/fODF based on the interpolated data [16,17]. Another approach is to directly interpolate the DT/dODF/fODF profiles

C. Seed point selection

In general, the integration procedure is performed on a number of seed points r_0 that define a specific 'region of interest' (ROI).Typically, these ROIs are defined by the user. This task requires anatomical knowledge and is subject to inter-operator variability. To reduce the operator dependence, ROIs can also be defined from atlas labels, or they can be obtained from cortical activation maps measured with functional MRI (fMRI). This last approach is particularly appealing since it allows for correlation analyses between structural and functional connectivity.

D. Tract-editing and clustering

Tract-editing is used to introduce prior anatomical knowledge of the fiber bundles in the brain, in order to refine the fiber-tracking results. In practice, tract-editing is performed by defining ROIs through which the tract is known to pass (also referred to as inclusive ROIs or AND gates). Tracts that enter these regions are considered anatomically plausible, and all other tracts are discarded. It is also possible to define regions through which the tracts are known not to pass and discard any tract that enters these regions (also referred to as exclusive ROIs or NOT gates). As an example, Figure II.4 (b) shows a successful 3D reconstruction of the cingulum bundle, by means of two AND gates. This technique has been successfully used to isolate and visualize many different WM bundles and as such it is sometimes referred to as 'in vivo virtual dissection'.

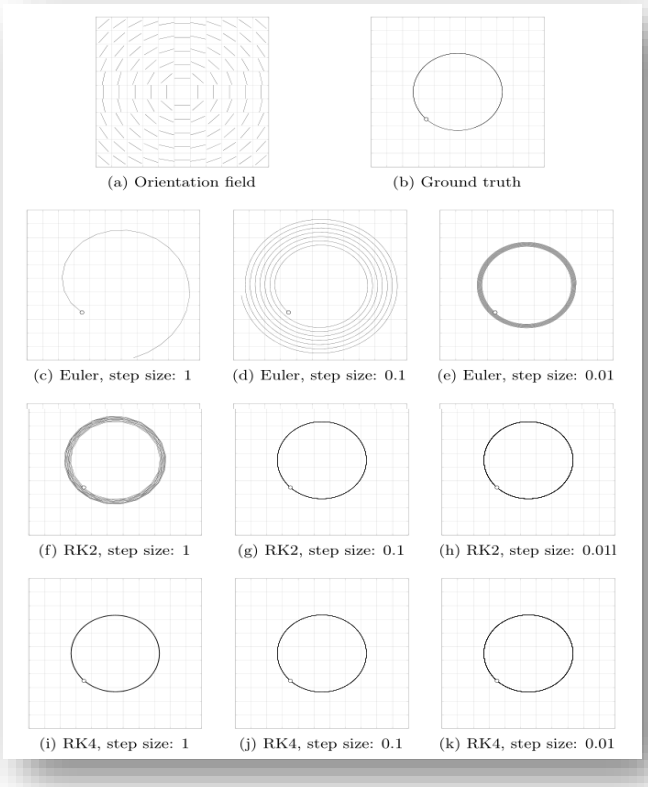

Figure II.2: *Euler vs. RK2 vs. RK4 integration for different step sizes. The seed point is indicated as a white dot. Note that, as we move away from the seed point, the integration errors accumulate. For Euler integration the accumulated error can become quite large, especially for large step sizes. Using higher order RK integration schemes, drastically reduces interpolation error made at each step, resulting in a much smaller accumulated error (even for relatively large step sizes).*

E. Tract termination

A final important aspect of streamline tractography is choosing when a tract should stop. Two criteria are commonly used: a threshold on the diffusion anisotropy and a curvature threshold. For example, in DTI tractography it is common to stop a streamline when the FA falls below a certain threshold value (typically FA < 0 . 2). The rationale behind this criterion is that regions of low FA tend to be associated with high uncertainty in the principal diffusion direction, and therefore a large potential error for the next streamline step. For tractography methods based on multi-fiber reconstruction algorithms, tracking is usually terminated when the dODF or fODF amplitudes along the current tracking orientation fall below a certain threshold [17,18]. The curvature threshold imposes a maximum local curvature of the tract: if the angle between two successive steps is above a predefined threshold, the tract is terminated. Since it is unusual to find bends in the white matter bundles that haveradii of curvature on the scale of an imaging voxel, any sudden change in trajectory is likely to be caused by artifacts such as noise.

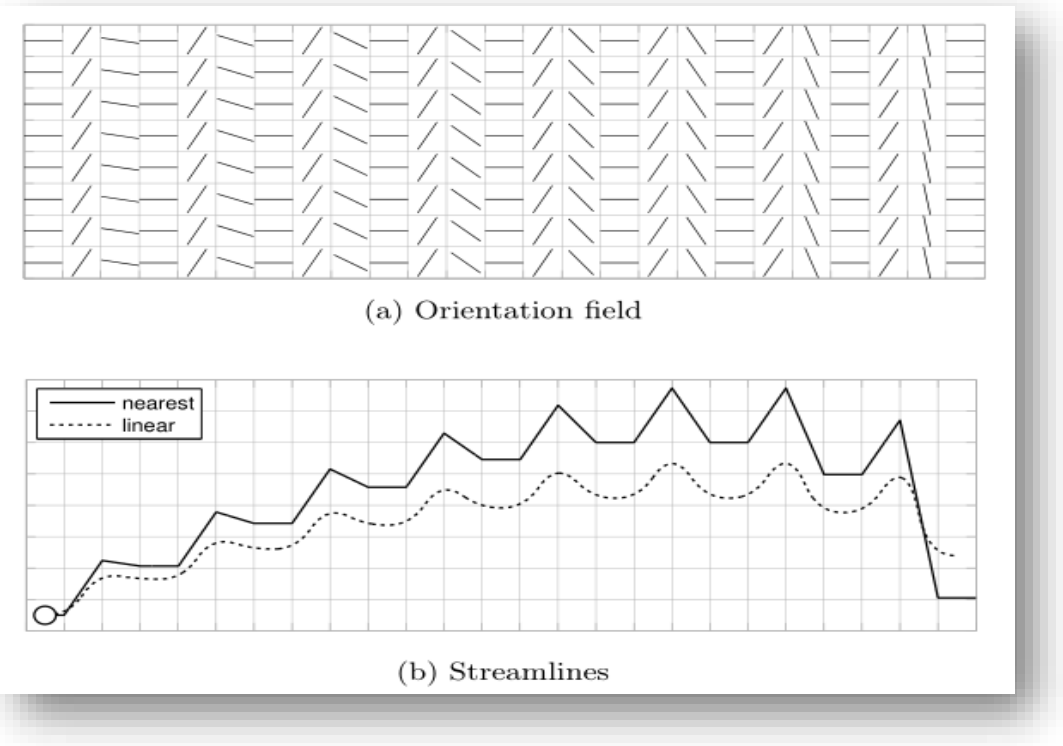

Figure II.3: *Nearest neighbor vs. linear interpolation. The seed point is indicated as a white dot. Note that, as we move away from the seed point, the errors made by the nearest neighbor interpolation accumulate*

F. Limitations

Deterministic streamline tractography is susceptible to three main sources of errors [19]. First, DWI is susceptible to imaging noise, which may cause a poor estimation of the dominant diffusion directions used in streamline tractography. As an example, Figure II.5 shows the variability of DTI fiber trajectories as a result of noise. Second, the microscopic anatomy of WM is bound to be more complex than what can be represented by the fiber reconstruction model. As such, streamline tractography is subject to modeling errors. This is especially true for tractography algorithms using the diffusion tensor model, which cannot resolve multiple fiber orientations inside one voxel. As an example, Figure II.6 shows the variability of DTI fiber trajectories as a result of modeling errors. Note that the uncertainty suddenly increases as soon as the trajectories enter regions of crossing fibers. Finally, streamline tractography is subject to integration errors. It is important to realize that all these errors will accumulate along the streamline (Figures II.5 and II.6).

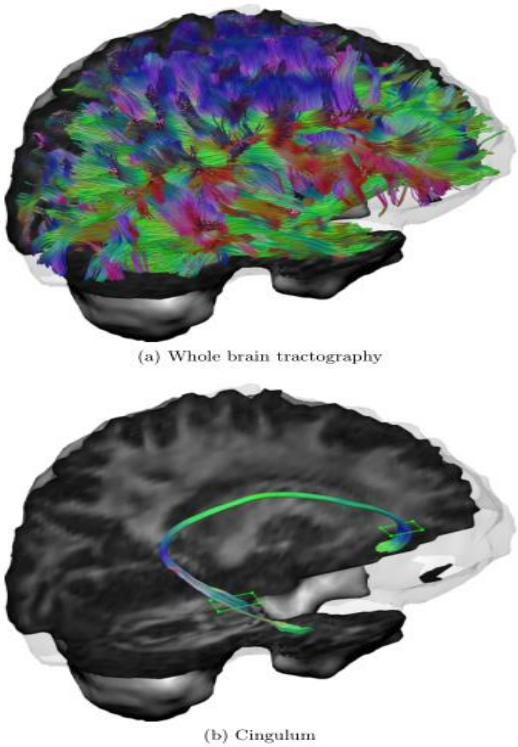

Figure II.4: *The cingulum bundle (b) is successfully extracted from whole brain tractography (a), using tract-editing with two AND gates (green rectangles).*

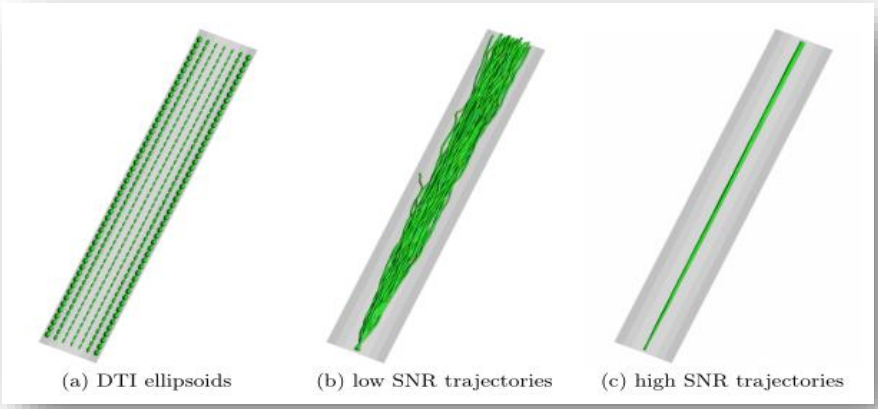

Figure II.5: *DTI tractography errors due to noise. A numerical phantom data set was constructed consisting of a single straight fiber bundle (a). Multiple trajectories where calculated for 100 noisy instances at low (b) and high (c) SNR.*

II.3. Probabilistic tractography

Deterministic tractography algorithms assume a unique fiber orientation estimate in each voxel and as such provide a single pathway emanating from each seed point (Figure II.7 a). However, as made clear in the previous section, the local fiber orientation estimates are subject to errors and uncertainty.

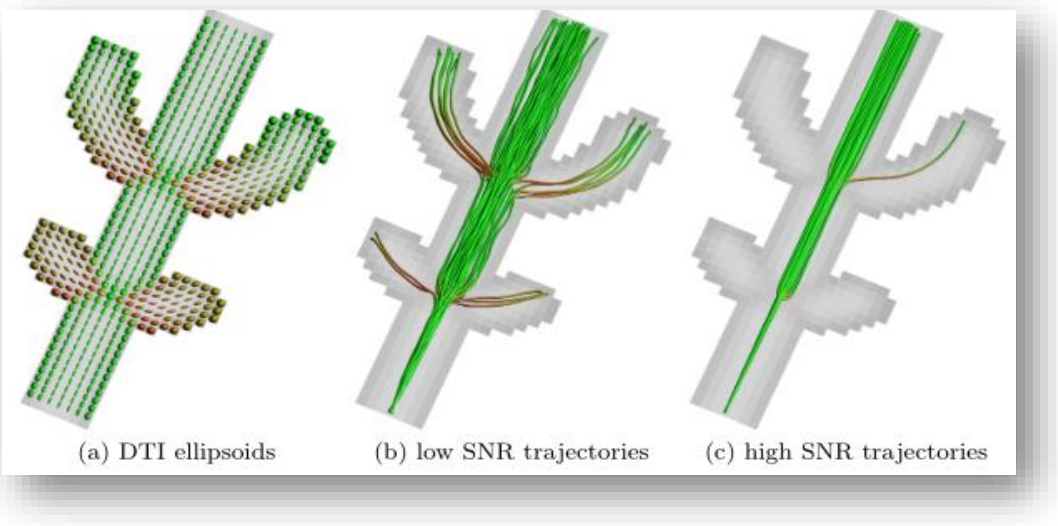

Figure II.6: DTI tractography errors due to noise and modeling errors. The numerical phantom data set of figure II.5 was extended with two regions of crossing fibers (a). Multiple trajectories where calculated for 100 noisy instances at low (b) and high (c) SNR. Note that, as the trajectories enter the region of crossing fibers, large modeling errors occur.

To characterize this uncertainty, probabilistic tractography algorithms generate a large collection or distribution of possible trajectories from each seed point (Figure II.7(b)). Brain regions that contain higher densities of the resulting trajectories are then deemed to have a higher probability of connection with the seed point [20, 21]. Probabilistic streamlines results are, therefore, often quantified by generating visitation count maps of the number of trajectories that traverse each voxel, which can then be analyzed and compared more readily (Figure II.7(c)) [19, 21].

By treating the problem in a probabilistic fashion, it also becomes possible to track through regions of high uncertainty, where deterministic techniques would usually stop, acknowledging, however, that the probability of connection beyond this region is lower. Typically, probabilistic tractography algorithms derive heavily from the deterministic streamline approach described in the previous section, and as such they are subject to the same limitations. The fundamental difference is that the orientations for tract propagation are drawn at random from a local uncertainty orientation density function (uODF) [22]. The main difference between the various probabilistic algorithms lies in how this uODF is constructed.

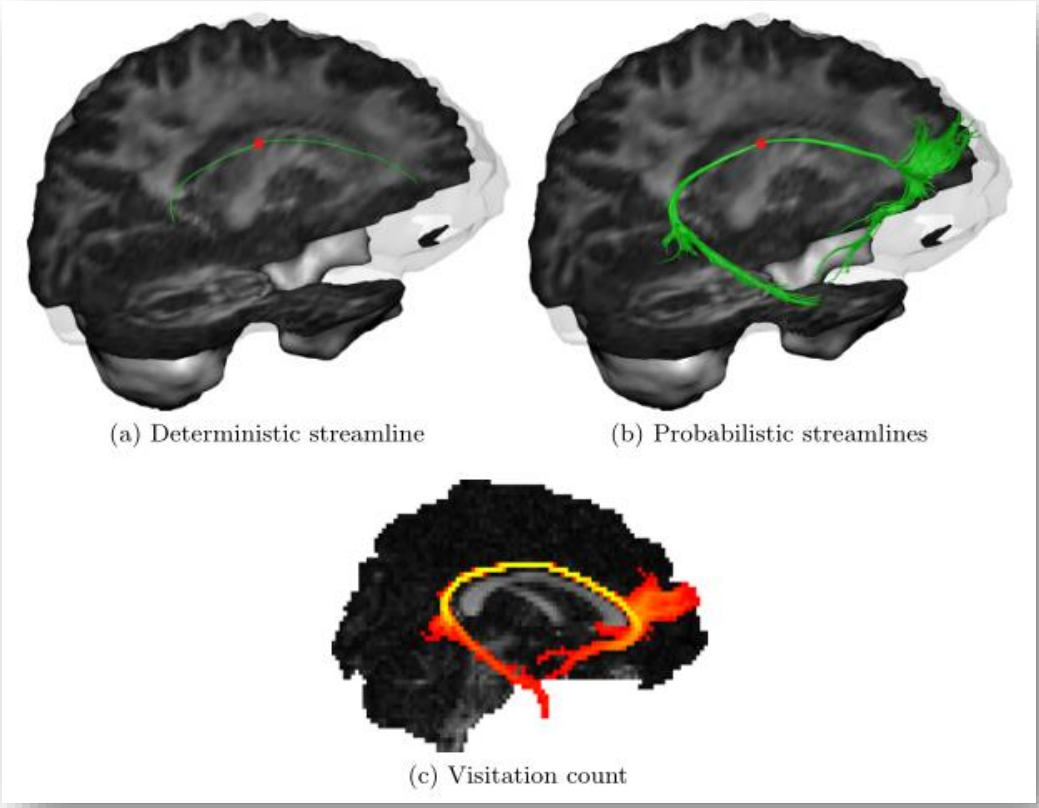

Figure II.7: Deterministic CSD streamline (a) vs. probabilistic streamlines (b) emanating from the same seed point (red sphere). From the probabilistic streamlines a visitation count map is often created (c), visualized here as a maximum intensity projection along the Y-axis.

A. Heuristic approaches

The earliest methods, based on DTI, relate the probability of a tract to the number of times it is reconstructed in a Monte Carlo random walk, where the characteristics of the random walk are determined by the shape of the underlying diffusion tensor [23[, [24], [25]. In voxels where there is no anisotropy, the generated vector is completely random. In anisotropic regions, the uODF is skewed to the axis of longest diffusion.

B. Rigorous approaches

To address the limitations of the heuristic approaches, more rigorous approaches were proposed that try to construct the true uODF.

- **Calibration approach:** instead of relying on a heuristic approach, some methods perform a calibration experiment to determine an empirical relationship between the features of the data and expected uODF [24, 26].
- **Bootstrap approach:** the bootstrap is a non-parametric statistical procedure that enables one to estimate the uncertainty of a given statistic, by randomly selecting individual measurements, with replacement, from a set of repeated measurements, thus generating many bootstrap realizations of the data. Each realization provides a random estimate of a given statistic. By generating a sufficient number of realizations, one obtains a measure of the uncertainty of a given statistic from the data itself without requiring a priori assumptions about the sources of uncertainty [27-29]. Bootstrapping has previously been combined with DTI tractography in order to produce probabilistic fiber trajectories [30, 31] However, in a clinical setting, even the small amount of repeated measurements to allow accurate and precise bootstrapping can render acquisition time unacceptably long [32, 33]. The problem of long acquisition times can be addressed using the residual bootstrap [34, 35]. This approach obtains probability distributions for model parameters by resampling residuals from a model fit (e.g., diffusion tensor fit). The huge advantage of this method is that it does not require repeated measurements, bringing acquisition time into the clinical range.

C. Global approaches

The previously mentioned tractography algorithms propagate the local fiber orientation estimates to obtain long-range fiber pathways. Recently, a number of tractography algorithms have been proposed based on a more global approach. Essentially, these algorithms attempt to find the configuration of fibers that best explains the observed data. As such, they do not rely on the preprocessing step to extract the fiber orientations, but rather operate directly on the acquired DW data, making tractography a one stage process. These methods rely on a model that predicts the DW signal intensities for a given arrangement of fiber orientations. These approaches have the potential to provide more robust results than current local streamlines methods. Unfortunately, these approaches are currently extremely computationally expensive limiting their immediate use in clinical environments.

II.4. Proposed Post-processing tractography:

Diffusion magnetic resonance imaging fiber tractography is a powerful tool for investigating human white matter connectivity in vivo. However, because of false fiber detection making interpretation of the tractography result is difficult. Optimal tractography must begin with an accurate description of the sub voxel white matter fiber structure. The output of tractography algorithms often contains spurious fibers, which are isolated and poorly aligned with the surrounding bundle of fibers. The fiber to bundle coherence (FBC) provides us with a quantitative measure of fiber alignment and is therefore useful in pruning the results of tractography algorithms by removing spurious fibers that are identified by a low FBC.

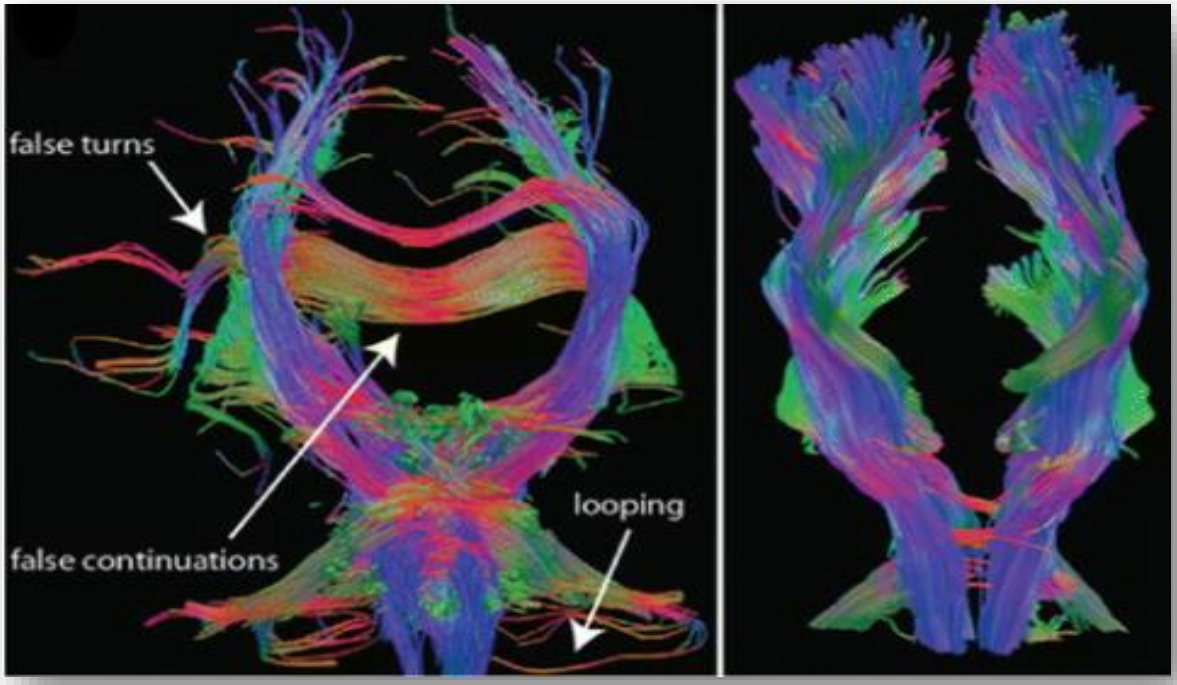

Figure II.8: *left: false brain imaging and right: expected brain imaging*

The false fibers outcome from errors, which is a combination start appearing from the data acquisition, passing from different methods of reconstruction and ends with different algorithms of tractography, this error is either increased from step to step or another error is produced in each step.

II.4.1. The proposed algorithm:

In this work, we propose to add another stage in the general flowchart which is the cleaning of the tractography results in order to obtain more realistic results implemented efficiently using multithreading and pre-computed lookup tables.

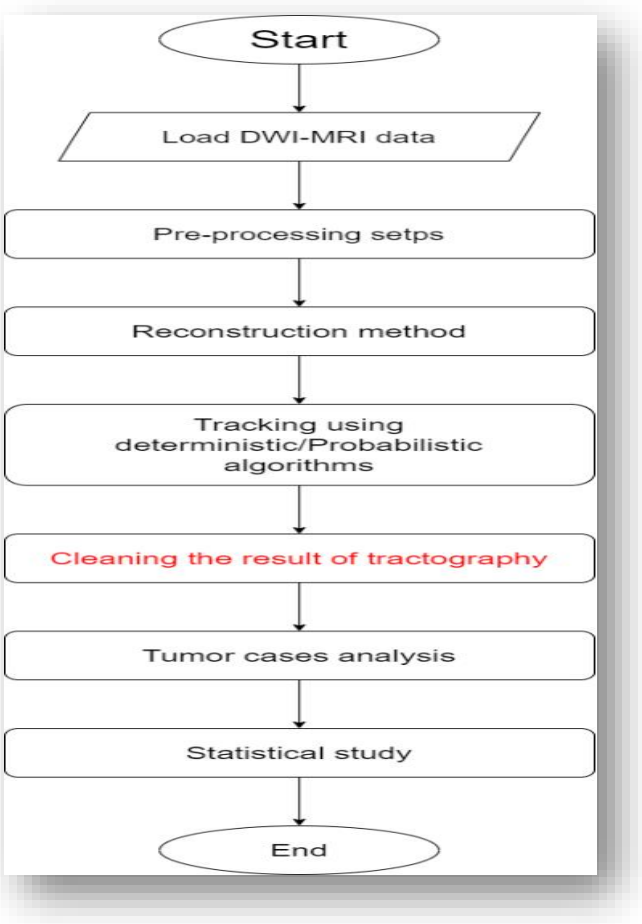

***Figure II.9**: Proposed Improvement of Tractography Algorithm*

II.4.2. Kernel density estimation:

In statistics, kernel density estimation (KDE) is a non-parametric way to estimate the probability density function of a random variable. Kernel density estimation is a fundamental data smoothing problem where inferences about the population are made, based on a finite data sample. In some fields such as signal processing and econometrics it is also termed the Parzen–Rosenblatt window method, after Emanuel Parzen and Murray Rosenblatt, who are usually credited with independently creating it in its current form. One of the famous applications of kernel density estimation is in estimating the class-conditional marginal densities of data when using a naive Bayes classifier, which can improve its prediction accuracy dramatically.

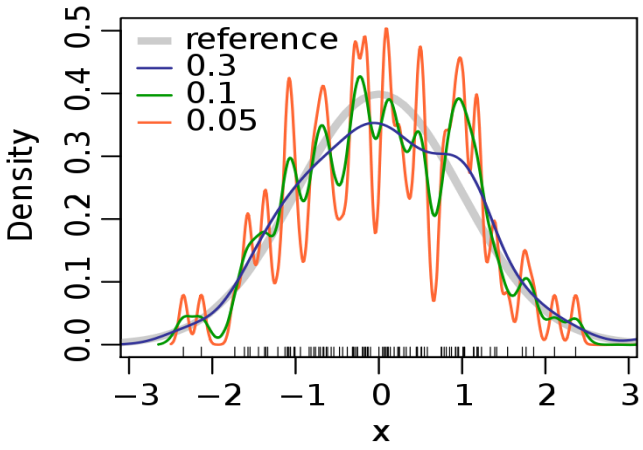

Figure II.10: *Kernel density estimation of 100 normally distributed random numbers using different smoothing bandwidths.*

A. Definition:

Let (x_1, x_2, …, x_n) be a univariate independent and identically distributed sample drawn from some distribution with an unknown density f. We are interested in estimating the shape of this function f. Its *kernel density estimator* is

$$\hat{f}_h(x) = \frac{1}{n}\sum_{i=1}^{n} K_h(x - x_i) = \frac{1}{nh}\sum_{i=1}^{n} K(\frac{x - x_i}{h}) \qquad \text{(II.10)}$$

Where K is the kernel - a non-negative function - and $h > 0$ is a smoothing parameter called the *bandwidth*. A kernel with subscript h is called the *scaled kernel* and defined as $K_h(x) = 1/h\ K(x/h)$. Intuitively one wants to choose h as small as the data will allow; however, there is always a trade-off between the bias of the estimator and its variance. The choice of bandwidth is discussed in more detail below.

A range of kernel functions are commonly used: uniform, triangular, biweight, triweight, Epanechnikov, normal, and others. The Epanechnikov kernel is optimal in a mean square error sense, though the loss of efficiency is small for the kernels listed previously. Due to its convenient mathematical properties, the normal kernel is often used, which means $K(x) = \phi(x)$, where ϕ is the standard normal density function.

The construction of a kernel density estimate finds interpretations in fields outside of density estimation. For example, in thermodynamics, this is equivalent to the amount of heat generated when heat kernels (the fundamental solution to the heat equation) are placed at each data point locations x_i. Similar methods are used to construct discrete Laplace operators on point clouds for manifold learning (e.g. diffusion map).

B. Lookup table:

In computer science, a **lookup table** is an array that replaces runtime computation with a simpler array indexing operation. The savings in terms of processing time can be significant, since retrieving a value from memory is often faster than undergoing an "expensive" computation or input/output operation. The tables may be precalculated and stored in static program storage, calculated (or "pre-fetched") as part of a program's initialization phase (memorization), or even stored in hardware in application-specific platforms. Lookup tables are also used extensively to validate input values by matching against a list of valid (or invalid) items in an array and, in some programming languages, may include pointer functions (or offsets to labels) to process the matching input. FPGAs also make extensive use of reconfigurable, hardware-implemented, lookup tables to provide programmable hardware functionality.

C. Lookup tables in image processing:

In data analysis applications, such as image processing, a lookup table (LUT) is used to transform the input data into a more desirable output format. For example, a grayscale picture of the planet Saturn will be transformed into a color image to emphasize the differences in its rings. A classic example of reducing run-time computations using lookup tables is to obtain the result of a trigonometry calculation, such as the sine of a value. Calculating trigonometric functions can substantially slow a computing application. The same application can finish much sooner when it first recalculates the sine of a number of values, for example for each whole number of degrees (The table can be defined as static variables at compile time, reducing repeated run time costs). When the program requires the sine of a value, it can use

	A	B	C
1	65535	65535	65535
2	65535	65535	65535
3	64193	62204	64123
4	62798	60068	62715
5	61567	58478	61487
6	60487	57206	60414
7	59529	56144	59466
8	58670	55230	58617
9	57891	54428	57849
10	57179	53713	57147
11	56523	53067	56501
12	55915	52478	55902
13	55348	51937	55345
65525	1	1	1
65526	1	1	1
65527	1	1	1
65528	1	1	1
65529	1	1	1
65530	0	1	0
65531	0	0	0
65532	0	0	0
65533	0	0	0
65534	0	0	0
65535	0	0	0
65536	0	0	0
65537			

Figure II.11: *Red (A), Green (B), Blue (C) 16 bit Look Up Table file sample. (Lines 14 to 65524 not shown)*

the lookup table to retrieve the closest sine value from a memory address, and may also take the step of interpolating to the sine of the desired value, instead of calculating by mathematical formula. Lookup tables are thus used by mathematics co-processors in computer systems. An error in a lookup table was responsible for Intel's infamous floating-point divide bug.

II.4.3. Fiber to bundle coherence measures:

The fiber to bundle coherence (FBC) quantitative measure of the alignment of each fiber with the surrounding fiber bundles [36]. These measures are useful in ‘cleaning’ the results of tractography algorithms, since low FBCs indicate which fibers are isolated and poorly aligned with their neighbors, as shown in the figure below.

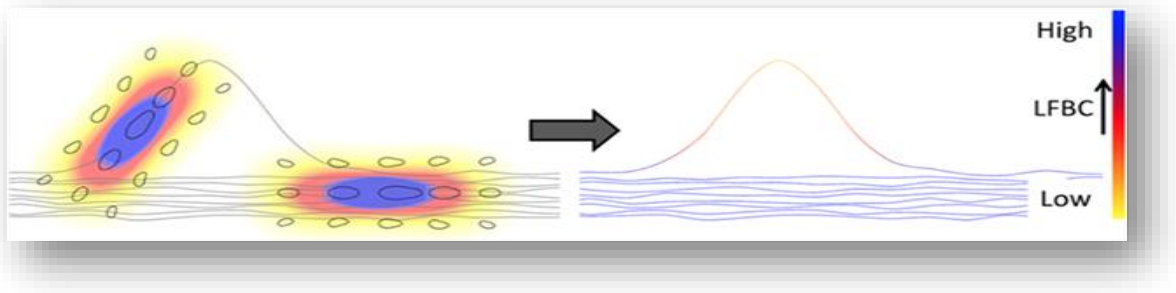

Figure II.12: *The contribution of two fiber points to the kernel density estimator.*

On the left this figure illustrates (in 2D) the contribution of two fiber points to the kernel density estimator. The kernel density estimator is the sum over all such locally aligned kernels. The local fiber to bundle coherence shown on the right color-coded for each fiber, is obtained by evaluating the kernel density estimator along the fibers. One spurious fiber is present which is isolated and badly aligned with the other fibers, and can be identified by a low LFBC value in the region where it deviates from the bundle. Figure adapted from Portegies [37].

II.4.4. Fiber to bundle coherence algorithm:

Here we implement FBC measures based on kernel density estimation in the non-flat 5D position-orientation domain. First, we compute the kernel density estimator induced by the full lifted output (defined in the space of positions and orientations) of the tractography. Then, the Local FBC (LFBC) is the result of evaluating the estimator along each element of the lifted fiber. A whole fiber measure, the relative FBC (RFBC), is calculated by the minimum of the moving average LFBC along the fiber. An example is illustrated in figure II.13.

Step 1:

- A lookup-table is created, containing rotated versions of the fiber propagation kernel rotated over a discrete set of orientations[38].
- In order to ensure rotationally invariant processing, the discrete orientations are required to be equally distributed over a sphere. By default, a sphere with 100 directions is used obtained from electrostatic repulsion in DIPY.

Step 2:

- The FBC measures are now computed, taking the tractography results and the lookup tables as input

Step 3:

- After calculating the FBC measures, a threshold can be chosen on the relative FBC (RFBC) in order to remove spurious fibers. Recall that the relative FBC (RFBC) is calculated by the minimum of the moving average LFBC along the fiber.

-

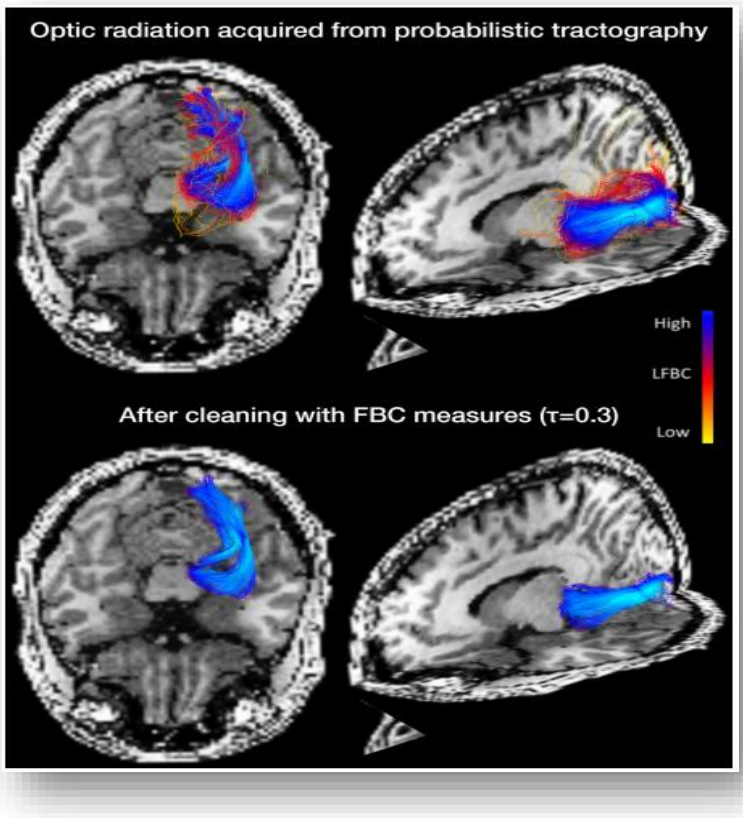

Figure II.13: *The fiber to bundle coherence (FBC) measures are demonstrated on the reconstruction of the optic radiation (OR). The OR can be obtained through probabilistic tractography by tracking fibers from the calcarine sulcus to the lateral geniculate nucleus (shown in top). The fibers are color-coded by the local FBC value (LFBC). The tractography result is cleaned (shown in bottom) by removing fibers with a relative FBC (RFBC) lower than the threshold τ=0.3.*

II.5. Summary:

In this chapter, we saw two different techniques of fibers tractography, that is, the deterministic one and the probabilistic one, the difference between them and the limitation of each one.

However, tractography is prone to generate spurious streamlines, which deviate strongly from neighboring streamlines, that's why we proposed an improvement by cleaning the results using fiber to bundle coherence (FBC) Algorithm.

CHAPTER III

Experiments & Results

III.1. Introduction

After introducing the new step added to the previous algorithm, a call for the software implementation is established. The program was implemented from scratch using Payton programming language including many libraries like nibabel, numpy, scipy, fury.

In this section we will present the dataset we used in our experiments, the different tools, software, programs and libraries that were used in the accomplishment of the experiments. And finally, we will present our results and discuss them.

III.2. Dataset:

The needed data was obtained from the UK dataset archive resumed in Table III.4 [39] and we have also used simulated data for further analysis.

III.3. Processing software:

Many software programs are available on the net to provide the user with a full support in dealing with 3D images, they run on different platforms and are all for free. The programs we used are listed below:

III.3.1. MI Brain:

` Is a program for viewing, processing and analyzing images from diffusion MRI developed by the Canadian firm Imeka in 2015. To date, it is used in the imaging laboratories of the University of Sherbrooke while awaiting its official launch planned in march 2016.

A. Characteristics:

MI-Brain allows you to view, edit, analyze images and perform real-time tractography of nerve fiber bundles from diffusion MRI images. This software offers the possibility of stacking images (open several images at the same time and superimpose them). There are a multitude of file formats that can be processed by MI-Brain: *fiber bundle file*, DWI, DICOM, NIfti, PGN, TIFF, GIF, JPEG. MI-Brain has tools to make a desired selection of bundles of nerve fibers from one ROI region of interest to another. In addition, it is possible to display fibers having a minimum and / or a maximum length (in mm). This technique is widely used in the field of neuroscience research.

B. Features:

MI-Brain can be handled via an interface of floating windows arranged side by side. The main window is divided into 3 main sections:

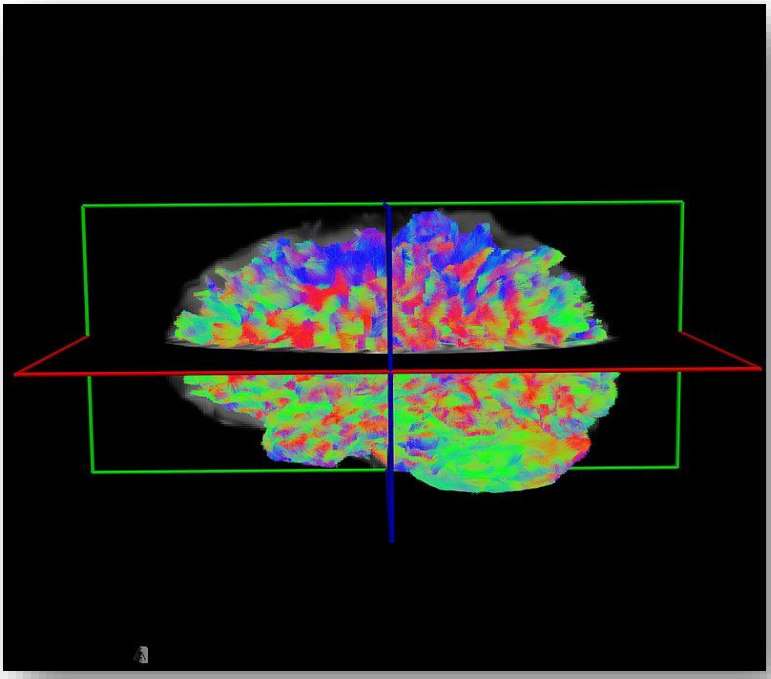

Figure III.1: *Tractography of an open human brain with MI-Brain.*

- **Left section:** Space of open files in MI-Brain®. ***At the top,*** we find the names of the files that are open (without extensions) provided, on the left, with a small solid square. To hide (hide) the display of an image or an object, just click on the small square which will appear, at this time, empty. ***At the bottom,*** there is the spatial information of the open image. You can navigate (move) in the space of the image, either by changing the numbers manually, or by scrolling the blue bar along the line in front of the name of the axis on which you want to move.
- **Middle section:** Four square sub-windows for viewing the different anatomical sections of the brain. the lower right section gives the 3D view of a volume (3D) image. The other three offer a 2D view. the top left sub-window offers an axial view, the top right window shows a sagittal view and finally the bottom left window is used to visualize the coronal slices.
- **Right section:** Analysis and image processing functions. The most used function is that which allows to select bundles of nerve fibers. This can be done either by placing selection boxes at determined locations, or by manually drawing, on the anatomical

structures, regions of interest which can be saved as a file. In both cases, the fiber bundles that pass only to those regions of interest (selection or drawn boxes) are displayed and are marked by color codes in relation to the anatomical view of each space:

1. *The **red** color:* It represents the left-right orientation. It marks the axial plane (top view).
2. *The **blue** color:* It represents the lower-upper orientation. It marks the coronal plane (front view).
3. *The **green** color:* It represents the front-back orientation. It marks the sagittal plane (side view).

These color codes facilitate better interpretation of images and help quickly recognize the orientation of fibers, images and objects in space.

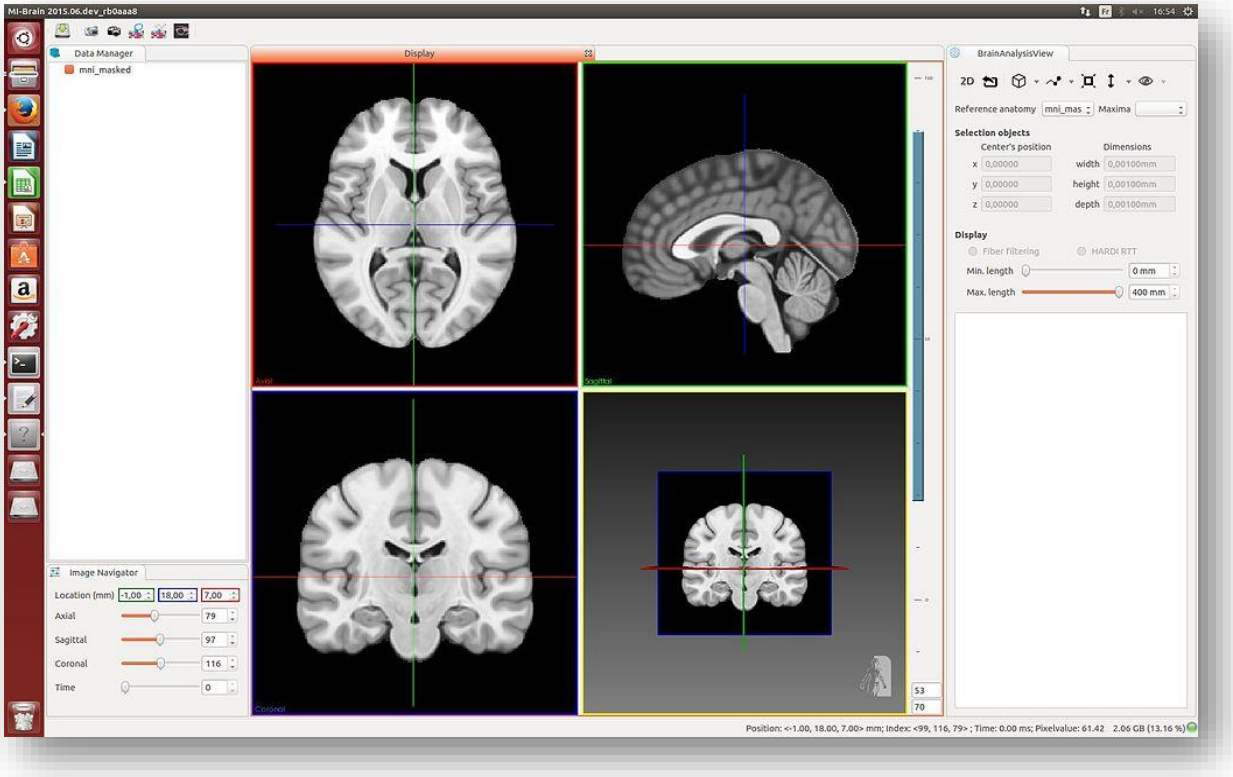

Figure III.2: *The midbrain views (superior (Axial), posterior (Coronal), lateral (Sagittal) and 3D views)*

III.3.2. Mango:

Mango is multi-image analysis GUI and a viewer for medical research images. It provides analysis tools and a user interface to navigate image volumes. The different features of the software is given as follow:

- Support for anal Analyze, DICOM, NEMA-DES, MINC, NIFTI and NIFTI2 image formats
- *Support:* VTK (legacy), GIFTI (.surf.gii) and BrainVisa surface formats.
- *Partial support*: TIFF, Concorde microPET, AFNI (legacy), Stimulate, and CTI ECAT.
- *Development:* Supports both Java Plugin API and Python Script API development.
- *Customizable:* Create custom filters, color tables, file formats, and atlases.
- *Command-line integration:* open and process images from the command-line.
- *Web:* Custom protocol and Papaya JavaScript viewer.
- *ROI Editing:* Threshold and component-based tools for painting and tracing ROIs.
- *Surface Rendering:* Interactive surface models supporting cut planes and overlays.
- *Image Registration:* Semi-automatic image co-registration and manual transform editing.
- *Image Stacking:* Threshold and transparency-based image overlay stacking.
- *Analysis:* Histogram, cross-section, time-series analysis, image and ROI statistics.
- *Processing:* Kernel and rank filtering, arithmetic/logic image and ROI calculators.

III.4. Tools and libraries used in the implementation of the program:

III.4.1. Python:

Python is an Interpreted, high-level, general-purpose programming language. Created by Guido van Rossum and first released in 1991, Python's design philosophy emphasizes code readability with its notable use of significant whitespace

III.4.2. DIPY:

DIPY is a **free** and **open source** software project for computational neuroanatomy, focusing mainly on **diffusion** *Magnetic Resonance Imaging* (dMRI) analysis, in another word is the paragon 3D/4D+ imaging library in Python. Contains generic methods for spatial normalization, signal processing, machine learning, statistical analysis and visualization of medical images. Additionally, it contains specialized methods for computational anatomy including diffusion, perfusion and structural imaging and It implements a broad range of algorithms for denoising, registration, reconstruction, tracking, clustering, visualization, and statistical analysis of MRI data.

III.4.3. NiBabel:

Read/write access to some common Neuroimaging file formats, this package provides read +/- write access to some common medical and Neuroimaging file formats, including: ANALYZE (plain, SPM99, SPM2 and later), GIFTI, NIfTI1, NIfTI2, CIFTI-2, MINC1, MINC2, AFNI BRIK/HEAD, MGH and ECAT as well as Philips PAR/REC. We can read and write FreeSurfer geometry, annotation and morphometry files. There is some very limited support for DICOM, NiBabel is the successor of PyNIfTI.

III.4.4. NumPy:

NumPy is a library for the Python programming language, adding support for large, multi-dimensional arrays and matrices, along with a large collection of high-level mathematical functions to operate on these arrays. The ancestor of NumPy, Numeric, was originally created by Jim Hugunin with contributions from several other developers. In 2005, Travis Oliphant created NumPy by incorporating features of the competing Numarray into Numeric, with extensive modifications. NumPy is open-source software and has many contributors.

III.4.5. Scipy:

Scipy is a free and open-source Python library used for scientific computing and technical computing. it contains modules for optimization, linear algebra, integration, interpolation, special functions, FFT, signal and image processing, ODE solvers and other tasks common in science and engineering. SciPy builds on the NumPy array object and is part of the NumPy stack which includes tools like Matplotlib, pandas and SymPy, and an expanding set of scientific computing libraries. This NumPy stack has similar users to other applications such as MATLAB, GNU Octave, and Scilab. The NumPy stack is also sometimes referred to as the SciPy stack.

III.5. Data file format:

Nifti stands for Neuroimaging Informatics Technology Initiative and it is an open file format commonly used to store brain imaging data obtained using Magnetic Resonance Imaging methods. In dipy, nifti data is a 4D array where the first 3 dimensions are the i, j, k voxel coordinates and the last dimension is the number of non-weighted (S0s) and diffusion-weighted volumes.

III.6. Region of interest:

A region of interest (often abbreviated ROI), are samples within a data set identified for a particular purpose. The concept of a ROI is commonly used in many application areas. For example, in medical imaging, the boundaries of a tumor may be defined on an image or in a volume, for the purpose of measuring its size. Dipy allows us to select a specific ROI from the streamlines obtained from the tractography by using the target tool which allows one to filter streamlines that either pass through or do not pass through some region of the brain.

- **Dipy's target tool:**

The target tool is a function that we used in order to filter out streamlines that pass through a specific region of interest. This function takes a set of streamlines and a region of interest (ROI) and returns only those streamlines that pass though the ROI

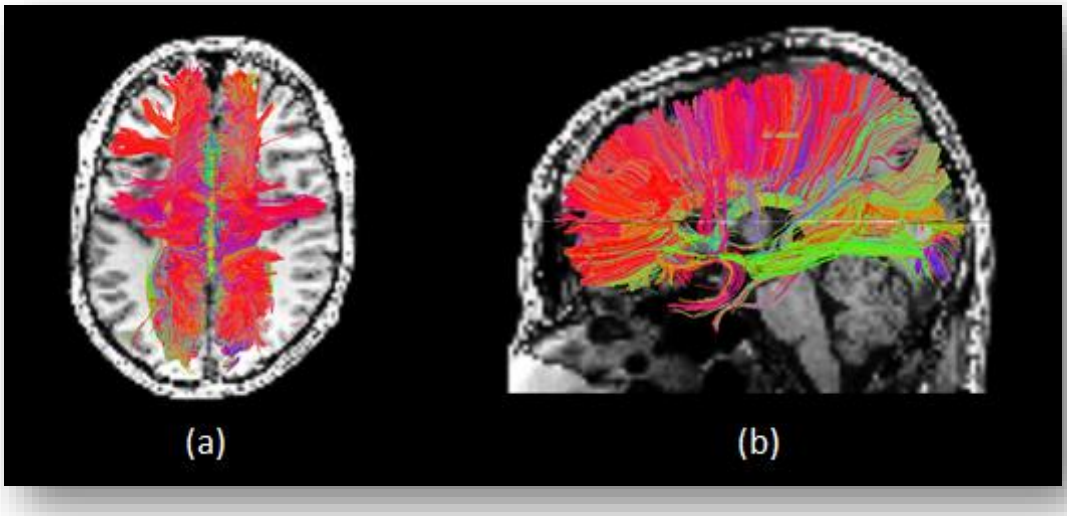

Figure III.3: *a) Corpus Callosum Axial b) Corpus Callosum Sagittal ROIs filtered using the target tool*

III.7. Description of the Program Operation:

We implement FBC measures based on kernel density estimation in the non-flat 5D domain. First, we compute the kernel density estimator induced by the full lifted output of the tractography. Then, the Local FBC (LFBC) results from evaluating the estimator along each element of the lifted fiber (Figure III.1). A whole fiber measure, the relative FBC (RFBC), is calculated by the minimum of the moving average LFBC along the fiber. The kernels used in the kernel density estimation have a probabilistic interpretation.

III.7.1. Experiment 1:

In this experiment, we describe an example illustrating the method which is performed on the Stanford HARDI dataset (150 orientations, b=2000s/mm^2). Constrained Spherical Deconvolution is used to create the fiber orientation density function, after which probabilistic tractography is applied. The spurious fibers identified by a low RFBC are removed by setting a threshold (τ=0.2). Regarding computation time, after a one-time computation of the lookup-table (taking several minutes) the fiber tracking followed by the FBC computation. The different steps are presented below:

- **Loading the data:** The FBC measures are evaluated on the Stanford HARDI dataset (150 orientations, b=2000 s/mm2*s/mm2*).
- **Selecting a region of interest:** Select a relevant part of the data (left hemisphere) coordinates given in x bounds, y bounds, z bounds this done with the help of mango software to extract the coordinates.
- **Fitting the data:** The data is first fitted to Constant Solid Angle (CDA) ODF Model. CSA is a good choice to estimate general fractional anisotropy (GFA). The stopping criterion can be used to restrict fiber tracking to those areas where the ODF shows significant restricted diffusion, thus creating a region-of-interest in which the computations are performed.
- **Fibers Reconstruction:** We first fit the data to the Constrained Spherical Deconvolution (CSD) model in DIPY. This model represents each Voxel in the data set as a collection of small white matter fibers with different orientations. The density of fibers along each orientation is known as the Fiber Orientation Distribution (FOD), used in the fiber tracking.
- **Tractography:** Local Tracking is used for probabilistic tractography which takes the direction getter along with the stopping criterion and seeds as input.
- **Lookup-table:** A lookup-table is created, containing rotated versions of the fiber propagation kernel Pt, regarding the kernel. In order to ensure rotationally invariant processing, the discrete orientations are required to be equally distributed over a sphere. By default, a sphere with 100 directions is used.

- **FBC measures:** After calculating the FBC measures, a threshold can be chosen on the relative FBC (RFBC) in order to remove spurious fibers. Recall that the relative FBC (RFBC) is calculated by the minimum of the moving average LFBC along the fiber. In this example we show the results for threshold 0 (i.e. all fibers are included) and 0.2 (removing the 20 percent most spurious fibers in this example).
- **Saving the result:** Finally, the streamlines obtained from the tractography are saved and can be now visualized using and visualization program like Mi-Brain. The tractography result is shown in figure III.4.

The tractography result is then cleaned by removing fibers with a relative FBC (RFBC) lower than the threshold τ=0.2 as illustrated in figure III.5.

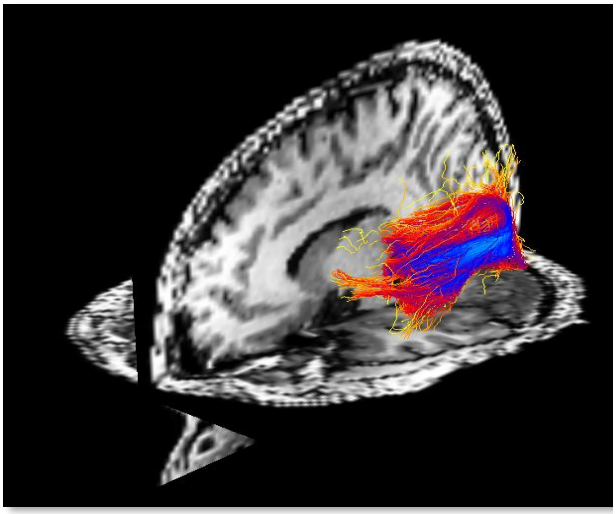

Figure III.4: *The optic radiation obtained through probabilistic tractography colored by local fiber to bundle coherence*

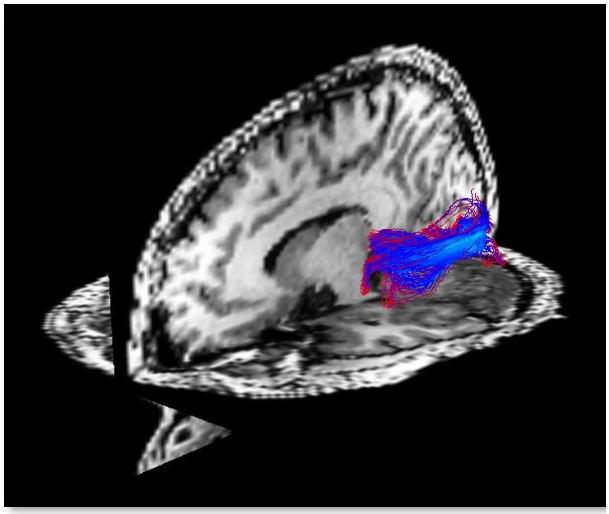

Figure III.5: *Cleaned tractography results based on the fiber to bundle measures.*

III.7.2. Experiment 2:

The program was run using different data varying from simulated and real ones normal and abnormal for the whole brain and separate regions of interest. It was tested several times using different methods of reconstruction and tractography varying the Generalized Fractional Anisotropy (GFA) and the threshold of cleaning τ. The results on the whole brain is given in the following tales:

Table III.1: *Results of Fiber tracking, before and after proposed Post-Processing with FBC using DTI reconstruction method.*

GFA	Reconstruction Method	Tractography Algorithm	τ	Number of Streamlines before	Number of Streamlines after
0.4	DTI	Deterministic	0.2	25231	23155
0.25	DTI	Probabilistic	0.3	62088	51244
0.2	DTI	Probabilistic	0.3	81203	70123

Table III.2: *Results of Fiber tracking, before and after proposed Post-Processing with FBC using CSD reconstruction method.*

GFA	Reconstruction Method	Tractography Algorithm	τ	Number of Streamlines before	Number of Streamlines after
0.4	CSD	Deterministic	0.2	35071	33219
0.25	CSD	Probabilistic	0.3	90401	79366
0.2	CSD	Probabilistic	0.3	160878	136001

Table III.3: *Results of Fiber tracking, before and after proposed Post-Processing with FBC using Q-Ball reconstruction method.*

GFA	Reconstruction Method	Tractography Algorithm	τ	Number of Streamlines before	Number of Streamlines after
0.4	Q-Ball	Deterministic	0.2	32547	29215
0.25	Q-Ball	Probabilistic	0.3	78620	50112
0.2	Q-Ball	Probabilistic	0.3	12594	10489

III.7.2. Experiment 3:

In this experiment, we have applied the different programs using CSD reconstruction method in the brain-damaged region and for that purpose, we have used five patients data obtained from the UK dataset archive resumed in Table III.4 [39], we have chosen the maximum number of streamlines near the Regions Of Interest (ROI).

Table III.4: *Summary of the clinical data used in the study*

Cases	**Pathology/ *Tumor location*/ Sex/ Age**
Case 1:	Astrocytoma type II (*Wemiche Area*), M/41years
Case 2:	Astrocytoma type II (*Left Temporal Cortex*), F/27 years
Case 3:	Astrocytoma type III (*Right Supplementory Motor Area)*, F/26 years
Case 4:	Glioblastoma Multiform (*Right Primay MotorArea)*, F/40years
Case 5:	Glioblastoma Multiform (*Right Primary Motor Area*), M/42 years

Table III.5: *Results of tracking cleaning with FBC, before and after proposed Post-Processing using CSD reconstruction method for the five different cases.*

Case	**GFA**	**Reconstruction Method**	**Tractography Algorithm**	**τ**	**Number of Streamlines before**	**Number of Streamlines after**
1	**0.2**	CSD	Probabilistic	0.3	41136	23541
2	**0.2**	CSD	Probabilistic	0.3	34418	19496
3	**0.2**	CSD	Probabilistic	0.3	39664	21496
4	**0.2**	CSD	Probabilistic	0.3	49631	31469
5	**0.2**	CSD	Probabilistic	0.3	35623	22367

The following figures present the visualization of the obtained result of the five cases using MI-Brain. The results of the tractography cleaning are saved and then loaded to MI-Brain software.

- ***Case 1:***

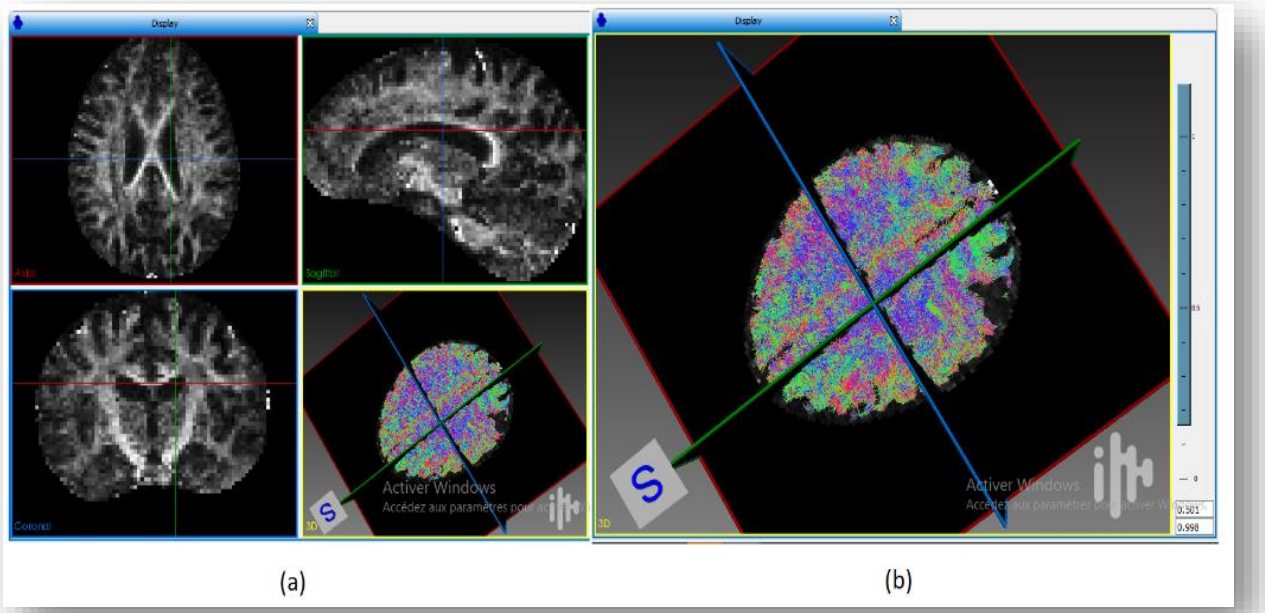

Figure III.6*: Visualization of Tractography results of the whole brain for case 1: a) Showing the brain matter along with the brain fibers. b) Focusing on the tractography results.*

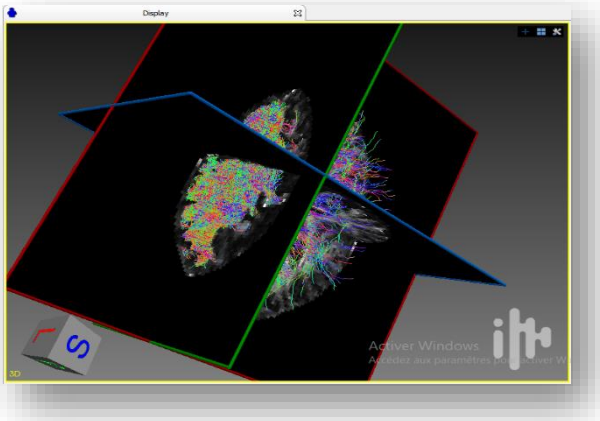

Figure III.7*: Visualization of Tractography results of the ROI (tumor area) fore case 1 before cleaning.*

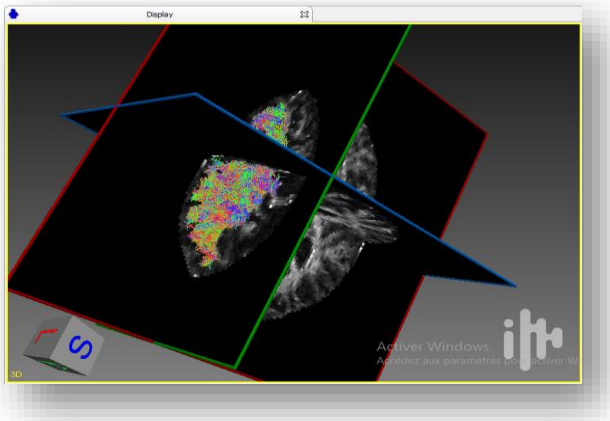

Figure III.8*: Visualization of the Tractography results of the ROI (tumor area) for case 1 after cleaning.*

- ***Case 2:***

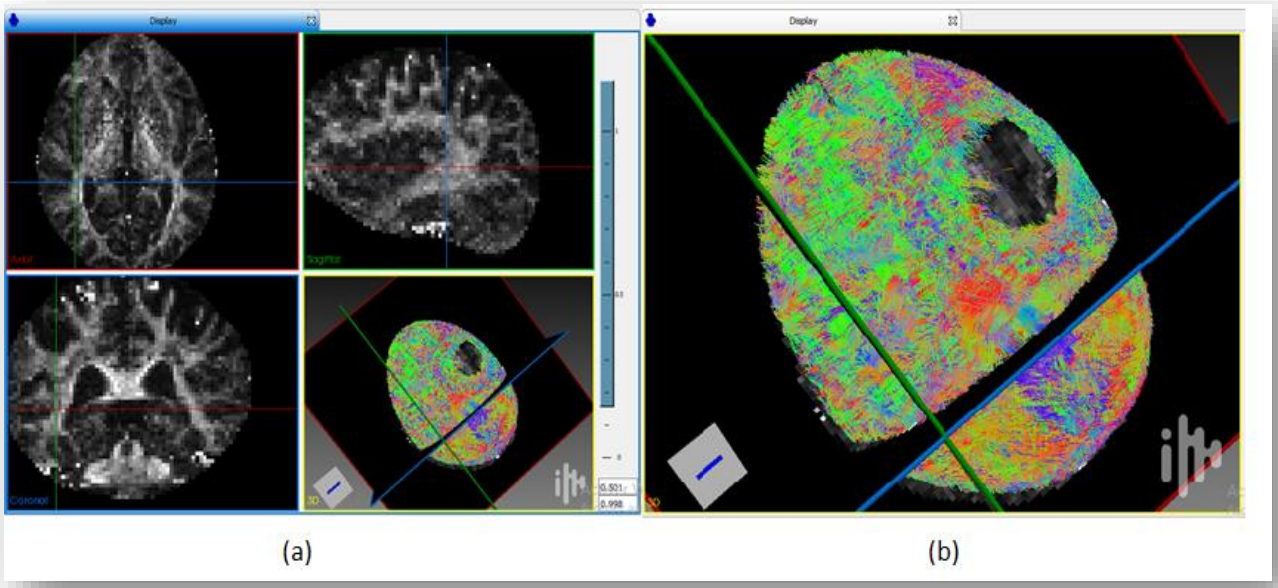

Figure III.9*: Visualization of tractography results of the whole brain for case 2: a) Showing the brain matter along with the brain fibers. b) Focusing on the tractography results.*

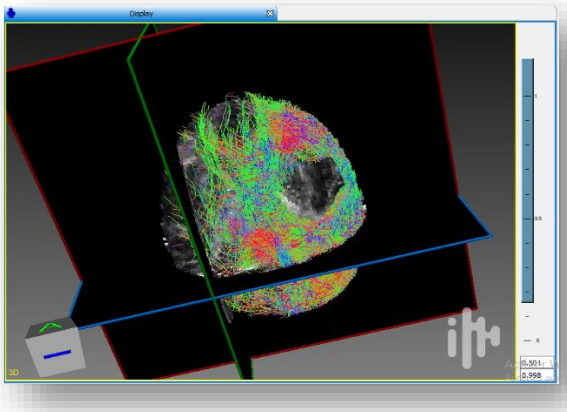

Figure III.10*: Visualization of tractography results of the ROI (tumor area) fore case 2 before cleaning.*

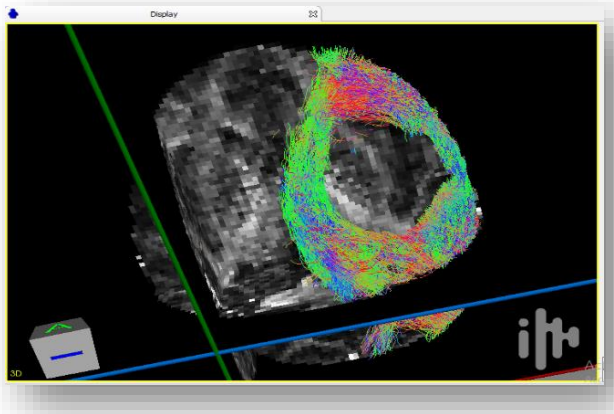

Figure III.11*: Visualization of the tractography results for the ROI (tumor area) for case 2 after cleaning.*

➢ ***Case 3:***

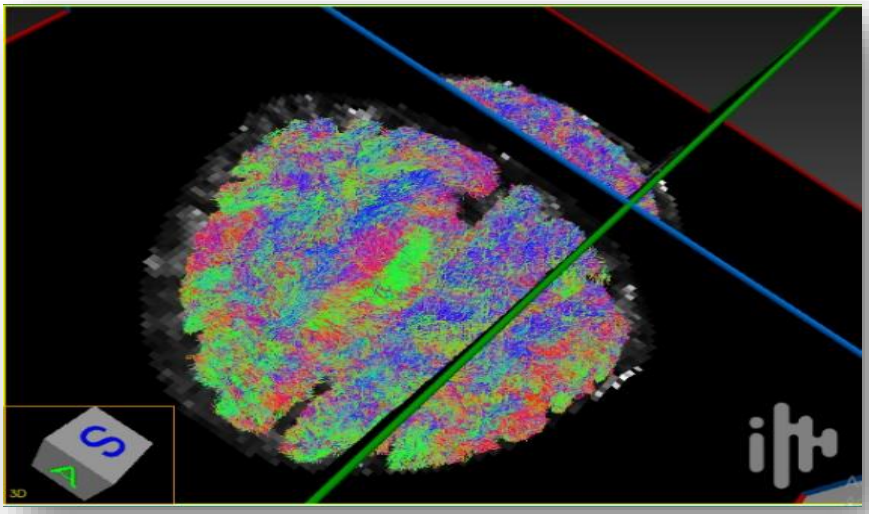

Figure III.12*: Visualization of tractography results of the whole brain for case 3.*

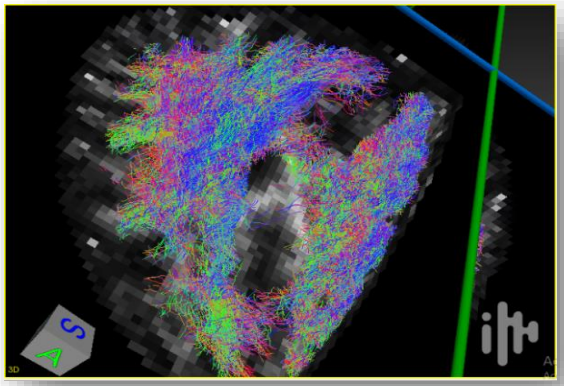

Figure III.13*: Visualization of tractography results of the ROI (tumor area) for case 3 before cleaning.*

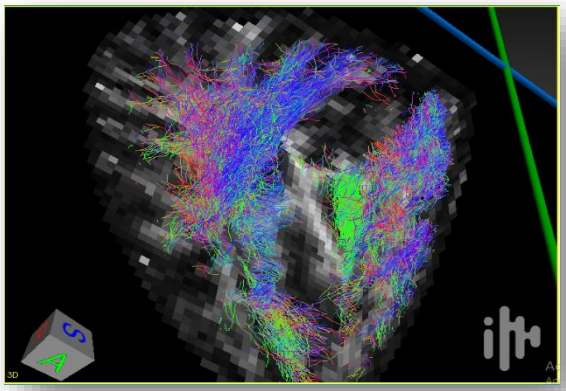

Figure III.14*: Visualization of the tractography results for the ROI (tumor area) for case 3 after cleaning.*

➢ ***Case 4:***

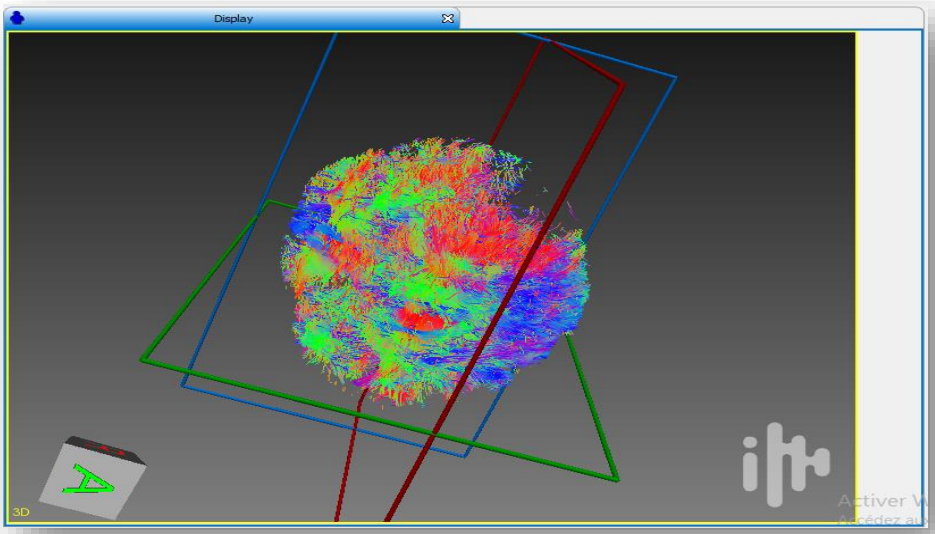

Figure III.15*: Visualization of tractography results of the whole brain for case 4.*

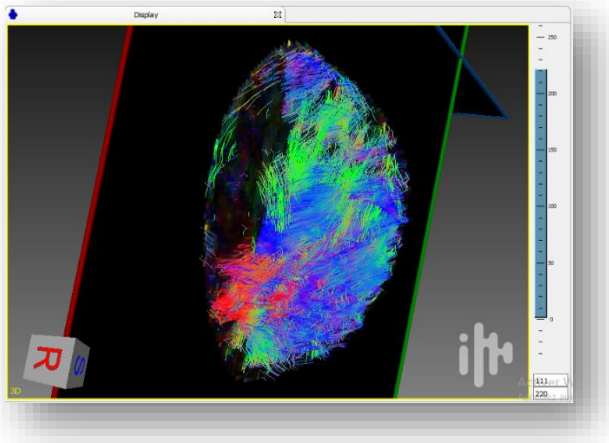

Figure III.16*: Visualization of tractography results of the ROI (tumor area) for case 4 before cleaning.*

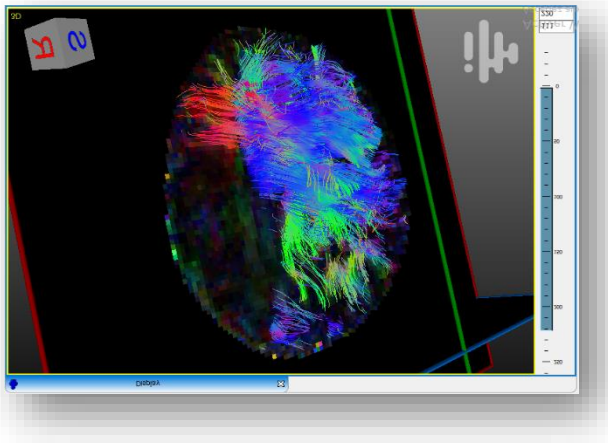

Figure III.17*: Visualization of the tractography results for the ROI (tumor area) for case 4 after cleaning.*

➢ ***Case 5:***

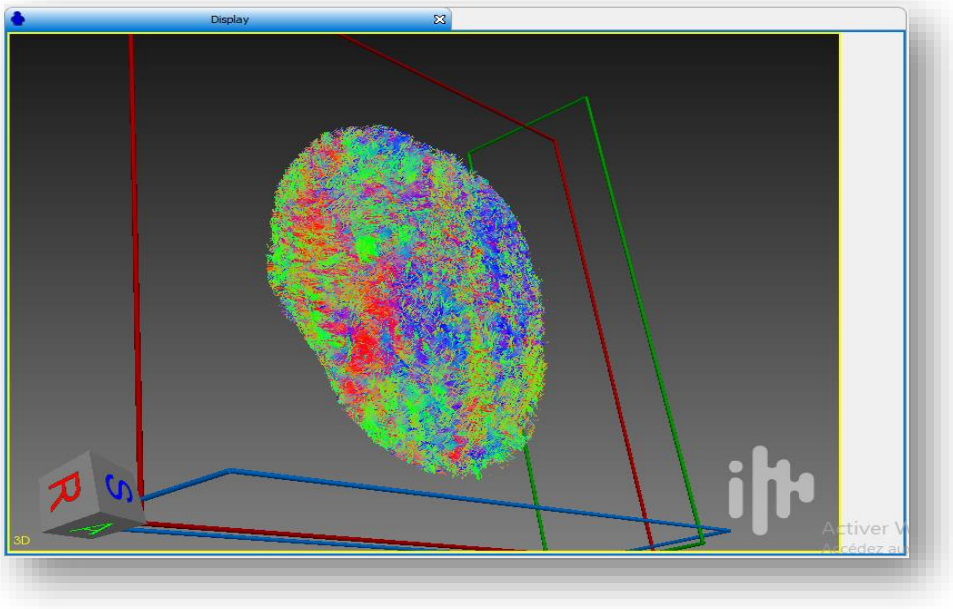

Figure III.18*: Visualization of tractography results of the whole brain for case 5.*

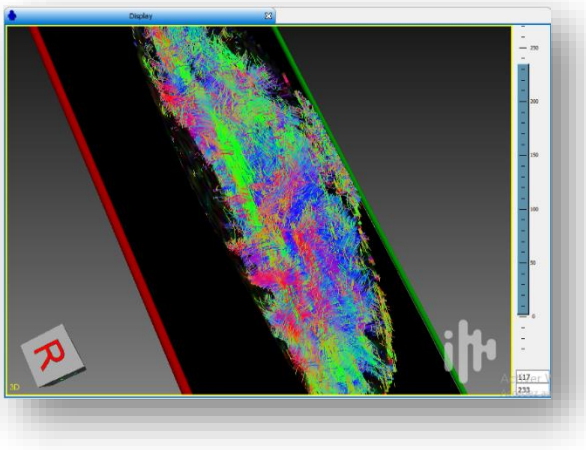

Figure III.19*: Visualization of tractography results of the ROI (tumor area) for case 5 before cleaning.*

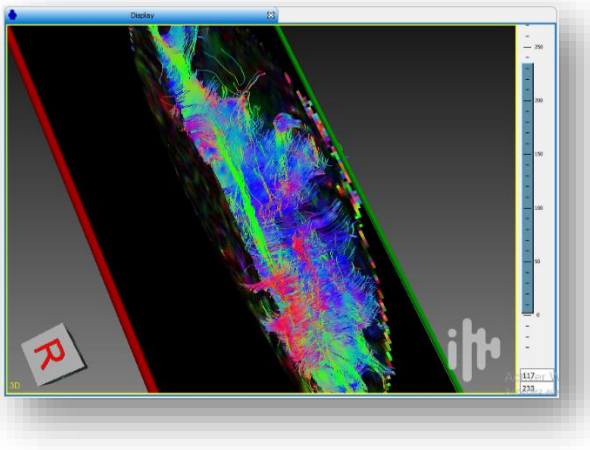

Figure III.20*: Visualization of the tractography results for the ROI (tumor area) for case 5 after cleaning.*

III.8. General discussion:

1. The increase of the b value improves the angular precision but in the same time produces more false fibers since the more we decrease GFA the more the peaks produced the more error produced in the acquisition, reconstruction and tractography steps. This is why we get more false fiber as we decrease GFA.
2. Changing the parameters in each step (acquisition, different methods of reconstruction and tractography) produces different brain images with different number of streamlines. The number of false fibers is due to noise caused by the acquisition and errors engendered in each step of reconstruction and tractography.
3. The new step added to the previous algorithm improves the final result by cleaning the tractography algorithm which removed the spurious fibers that are poorly aligned with their neighbors.
4. The results show that the visualization of the brain fibers is clearly improved especially when dealing with abnormal cases where it leads to a better detection of the tumor that results in clearer coordinates. This is mainly caused by the suppression of the false fibers that were confusing and perturbing the tumor's borders.
5. Choosing a region of interest gives a better study statistic for a specific region in the brain such as a tumor with abnormal data and it requires less time and resources to output the result.

III.9. Summary

In this chapter we carried the previous work of our colleagues and presented an updated version of the tractography algorithm which consists in cleaning the result of tractography. The output of tractography algorithms often contains spurious fibers which are isolated and poorly aligned with the surrounding bundle of fibers. The fiber to bundle coherence (FBC) provides us with a quantitative measure of fiber alignment and is therefore useful in pruning the results of tractography algorithms by removing spurious fibers and facilitating the processing of raw data obtained from MRI, with different visualization options in 3d. Moreover, a statistical study was performed in both real and simulated data with different brain states including tumors. The analysis was carried by changing different parameters to note the difference between each case and the effect of these parameters on the results. Therefore, getting a visualization of five brain cases with abnormal tissues.

GENERAL CONCLUSION & FURTHER WORK

General Conclusion & Further Work

This objective of this project was to propose an algorithm to enhance the tractography process and improve its results.

This work required some background knowledge on cerebral white matter anatomy and diffusion MRI principles. All these topics were reviewed and covered in the first chapter.

We first presented different reconstruction methods used to detect diffusion directions in the brain starting by DTI and showing its limitations in detecting multiple fibers crossings, then we introduced more efficient algorithms known as HARDI and discussed the solutions that were proposed to overcome these limitations. After that, we saw two main algorithms, probabilistic and deterministic, used in the tractography to visually represent fibers tracts.

Afterwards, we proposed an algorithm that was is able to improve the tractography algorithm by cleaning the results and removing the spurious algorithm to get clearer visualization of the whole brain or a specific region of interest. We have run our algorithm on different datasets with different brain states including abnormalities. We were able to successfully apply the algorithm on the different cases and visualized them using the Mi-Brain software. A statistical study was performed to analyze and compare between the different results and show the effect of the FBC technique using different parameters and reconstruction methods. We finally were able to get better visualization of the brain especially the ones including abnormalities where the reduction of the spurious fibers produced more defined borders of the tumors.

As further work, parallelism (multiprocessing) can be used to speed up the signal reconstruction process and hence resulting in a more efficient algorithm. Since the whole process of reconstruction and tractography usually takes a considerable amount of time, it can be reduced by optimizing the algorithm such that the voxels can be processed in parallel.

BIBLIOGRAHY

Bibliography

[1] R. Brown, "A brief account of microscopical observations made in the months of June, July and August, 1827, on the particles contained in the pollen of plants; and on the general existence of active molecules in organic and inorganic bodies" *Phil. Mag.* vol.4, pp. 161–173, 1828.

[2] A. Fick, "On liquid diffusion" Philos. Mag. J. Sci. vol. 10, pp. 31–39, 1855.

[3] A. Einstein, *Investigations on the Theory of the Brownian Movement*. Dover Pubns, 1956.

[4] M. Cercignani and M. Horsfield, "The physical basis of diffusion-weighted MRI" *J. Neurol.*, vol. 186, pp. 11–14, 2001.

[5] E. Stejskal and J. Tanner, "Spin diffusion measurements: spin echoes in the presence of a time-dependent field gradient" *Journal of Chemical Physics*, vol.42, pp.288–292, 1965.

[6] P. T. Callaghan, *Principles of nuclear magnetic resonance microscopy*. Oxford: Oxford University Press, 1991.

[7] Callaghan, P. T., C. D. Eccles, and Y. Xia, "RAPID COMMUNICATION: NMR microscopy of dynamic displacements: k-space and q-space imaging" Journal of Physics E Scientific Instruments, vol. 21, pp. 820–822, 1988.

[8] Hagmann, L. Jonasson, P. Maeder, J.-P. Thiran, V. J. Wedeen, and R. Meuli, "Understanding Diffusion MR Imaging Techniques: From Scalar Diffusion-Weighted Imaging to Diffusion Tensor Imaging and Beyond" *RadioGraphics* vol. 26, pp. 205–223, 2006.

[9] [9] D. Tuch, J. Belliveau, T. Reese, and V. Wedeen, "High Angular Resolution Imaging of the Human Brain" in *Proceedings of the International Society for the Magnetic Resonance in Medicine*. Philadelphia, pp. 321, 1999.

[10] D. Tuch, "Diffusion MRI of Complex Tissue Structure". Ph.D. thesis, Harvard

University and Massachusetts Institute of Technology, 2002

[11] D. Tuch, “Q-Ball Imaging”. *Magnetic Resonance in Medicine*, vol. 52, no. 6, pp. 1358–1372, 2004.

[12] S. Mori and P. C. M. Van Zijl “Fiber tracking: principles and strategies-a technical review” *NMR in Biomedicine*, vol. 15, no.7, 8, pp. 468–480, 2002.

[13] S. Mori, B. J. Crain, V. P Chacko, and P. Van Zijl, “Three-dimensional tracking of axonal projections in the brain by magnetic resonance imaging” *Annals of Neurology*, vol. 45, no. 2, pp. 265–269, 1999.

[14] R. Xue, P. van Zijl, B. J. Crain, M. Solaiyappan, and S. Mori, “In vivo three-dimensional reconstruction of rat brain axonal projections by diffusion tensor imaging” *Magnetic Resonance in Medicine*, vol. 42, no. 6, pp. 1123–1127, 1999.

[15] M. Lazar and A. L. Alexander, “An error analysis of white matter tractography methods: synthetic diffusion tensor field simulations” *NeuroImage*, vol.20, no.2, pp. 1140–1153, 2003.

[16] T. E. Conturo, N. F. Lori, T. S. Cull, E. Akbudak, A. Z. Snyder, J. S. Shimony, R. C. McKinstry, H. Burton, and M. E. Raichle “Tracking neuronal fiber pathways in the living human brain” *Proceedings of the National Academy of Sciences of the United States of America*, vol. 96, no. 18, pp. 10422–10427, 1999.

[17] B. Jeurissen , A. Leemans, D. K. Jones, J. D. Tournier, and J. Sijbers "Probabilistic fiber tracking using the residual bootstrap with constrained spherical deconvolution” *Human Brain Mapping*, vol. 32, pp. 461–479, 2011.

[18] M. Descoteaux, R. Deriche, TR Knösche, and A. Anwander “Deterministic and probabilistic tractography based on complex fibre orientation distributions” *IEEE Transactions on Medical Imaging*, vol. 28, no. 2, pp. 269–286, 2009.

[19] T. E. J. Behrens and S. Jbabdi, “MR diffusion tractography” in *Diffusion MRI: from quantitative measurement to in vivo neuroanatomy*. Cambridge, Massachusetts: Academic Press, pp. 333-351, 2009.

[20] T. E. J. Behrens, M. W. Woolrich, M. Jenkinson, H. Johansen-Berg, R. G. Nunes, S. Clare, P. M. Matthews, J. M. Brady, and S. M. Smith, "Characterization and propagation of uncertainty in diffusion-weighted MR imaging" *Magnetic Resonance in Medicine*, vol. 50, no. 5, pp. 1077–1088, 2003.

[21] G. J. M. Parker, H. A. Haroon, and C. A. M. Wheeler-Kingshott, "A framework for a streamline-based probabilistic index of connectivity (PICo) using a structural interpretation of MRI diffusion measurements" *Journal of Magnetic Resonance Imaging*, vol. 18, no. 2, pp. 242–254, 2003.

[22] K. K. Seunarine and D. C. Alexander, "Multiple fibers: beyond the diffusion tensor" in *Diffusion MRI: from quantitative measurement to in vivo neuroanatomy*. Cambridge, Massachusetts: Academic Press, pp. 55–72, 2009.

[23] M. Lazar and A. L. Alexander, "White matter tractography using random vector (RAVE) perturbation" in *Proceedings of the International Society for Magnetic Resonance in Medicine*. Honolulu, USA, vol. 10, pp. 539, 2002.

[24] G. J. M. Parker and D. C. Alexander "Probabilistic Monte Carlo based mapping of cerebral connections utilising whole-brain crossing fibre information" in *Proceedings of the International Conference on Information Processing in Medical Imaging*. Lake District, United Kingdom, pp. 684–695, 2003.

[25] J. D. Tournier, F. Calamante, D. G. Gadian, and A. Connelly, "Diffusion-weighted magnetic resonance imaging fibre tracking using a front evolution algorithm" *NeuroImage*, vol. 20, no. 1, pp. 276–288, 2003.

[26] G. J. M. Parker and D. C. Alexander, "Probabilistic anatomical connectivity derived from the microscopic persistent angular structure of cerebral tissue", *Philosophical Transactions of the Royal Society B: Biological Sciences*, vol. 360, no. 1457, pp. 893, 2005.

[27] B. Efron, "Bootstrap methods: another look at the jackknife" *The Annals of Statistics*, vol. 7, no. 1, pp. 1–26, 1979.

[28] D. K. Jones, “Determining and visualizing uncertainty in estimates of fiber orientation from diffusion tensor MRI” *Magnetic Resonance in Medicine*, vol. 49, no. 1, pp. 7–12, 2003.

[29] S. Pajevic and P. J. Basser. “Parametric and non-parametric statistical analysis of DT-MRI data” *Journal of Magnetic Resonance*, vol. 161, no. 1, pp. 1–14, 2003.

[30] D. K. Jones and C. Pierpaoli, “Confidence mapping in diffusion tensor magnetic resonance imaging tractography using a bootstrap approach” *Magnetic Resonance in Medicine*, vol. 53, no. 5, pp. 1143–1149, 2005.

[31] M. Lazar and A. L. Alexander, “Bootstrap white matter tractography (BOOT-TRAC)” *NeuroImage*, vol. 24, no. 2, pp. 524–532, 2005.

[32] R. L. O’Gorman and D. K. Jones, “Just how much data need to be collected for reliable bootstrap DT-MRI?” *Magnetic Resonance in Medicine*, vol. 56, no. 4, pp. 884–890, 2006.

[33] B. Jeurissen, A. Leemans, J. D. Tournier, and J. Sijbers “Bootstrap methods for estimating uncertainty in Constrained Spherical Deconvolution fiber orientations” in *Proceedings of the International Society for Magnetic Resonance in Medicine*. Toronto, Canada, vol. 16, pp. 3324, 2008,

[34] S. W. Chung, Y. Lu, and R. G. Henry, “Comparison of bootstrap approaches for estimation of uncertaintiesof DTI parameters” *NeuroImage*, vol. 33, no. 2, pp. 531–541, 2006.

[35] B. Whitcher, D. S. Tuch, J. J. Wisco, A. G. Sorensen, and L. Wang “Using the wild bootstrap to quantify uncertainty in diffusion tensor imaging” *Human Brain Mapping*, vol. 29, no. 3, pp. 346–362, 2007.

[36] S. Meesters, G. Sanguinetti, E. Garyfallidis, J. Portegies, P. Ossenblok, R. Duits. (2016) “Cleaning output of tractography via fiber to bundle coherence, a new open source implementation” *Human Brain Mapping Conference*, 2016.

[37] J. Portegies, R. Fick, G. Sanguinetti, S. Meesters, G.Girard, and R. Duits, "Improving Fiber Alignment in HARDI by Combining Contextual PDE flow with Constrained Spherical Deconvolution". *PLoS One*, 2015.

[38] R. Duits and E. Franken, "Left-invariant diffusions on the space of positions and orientations and their application to crossing-preserving smoothing of HARDI images" *International Journal of Computer Vision*, vol. 92, pp. 231-264, 2011.

[39] C. R Pernet, K. J. Gorgolewski, D. Job, D. Rodriguez, I. Whittle, & J. Wardlaw, *A structural and functional magnetic resonance imaging dataset of brain tumour patients*. [Data Collection]. Colchester, Essex: UK Data Archive, 2016. 10.5255/UKDA-SN-851861.

[40] P. Basser, J. Mattiello and D. LeBihan, "MR Diffusion Tensor Spectroscopy and imaging" *Biophysical Journal*, vol. 66, no. 1, pp. 259–267, 1994

[41] C. Westin C., S. Maier, H. Mamata, A. Nabavi, F. Jolesz, and R. Kikinis: "Processing and Visualization for Diffusion Tensor MRI" *Medical Image Analysis, vol.* 6, no. 2, pp. 93–108, 2002.